

# **Universidad de Santiago de Compostela**



## **Estimación de las Intensidades de los Núcleos Radioactivos producidos en el Super-FRS en la Futura Instalación del GSI**

## **Estimate Of The Intensities Of The Radioactive Nuclides Produced At The Super-FRS At The Future GSI Facility**

**Memoria del Trabajo de Investigación titulado enmarcado en los cursos  
de doctorado del programa de física de partículas y dinámica no lineal**

**Maria Valentina Ricciardi**

**Junio 2004**



# Contents

<b>Introducción</b> (en español)	<b>1</b>
<b>Introduction</b>	<b>3</b>
<b>1 The GSI Future Project</b>	<b>5</b>
1.1 The GSI Future Project	5
1.2 Physical Goals	9
1.2.1 Research with Rare-Isotope Beams – Nuclei far from stability	9
1.2.2 Research with Antiprotons – Hadron Spectroscopy and Hadronic Matter	11
1.2.3 Nucleus-nucleus collisions at high energy – Compressed Nuclear Matter	12
1.2.4 Ion Beam and Laser Beam Induced Plasmas – High Energy Density in Bulk Matter	13
1.2.5 Quantum Electrodynamics, Strong Fields, and Ion-Matter Interactions	14
1.3 Safety Aspects for Design and Operation of the New Facility	14
<b>2 The Superconducting Fragment Separator</b>	<b>17</b>
2.1 Basic principles of the Fragment Separator (FRS)	17
2.2 The Superconducting Fragment Separator (Super-FRS)	23
<b>3 Implementation of the ABRABLA code for the estimation of the RIB intensities at the Super-FRS entrance</b>	<b>27</b>
3.1 Introduction	27
3.2 The abrasion model in ABRABLA	30
3.3 The ablation model in ABRABLA	32
3.3.1 The evaporation model	32
3.3.2 The fission model	33

3.4	The kinematics of the nucleus-nucleus collision	35
3.5	Limitations and applicability of the ABRABLA code for radioprotection purposes	37
<b>4</b>	<b>Results and discussion</b>	<b>40</b>
4.1	Analysis of the data	40
4.2	Results	44
4.3	Discussion	54
	<b>Conclusions</b>	<b>63</b>
	<b>Conclusión</b> (en español)	<b>65</b>
	<b>Bibliography</b>	<b>67</b>

# Introducción

En febrero del 2003, el gobierno federal alemán aprobó la propuesta para la construcción de un “Acelerador Internacional para Haces de Iones y Antiprotones”. La futura instalación estará situada en Darmstadt, Alemania, y representa una extensión del actual laboratorio GSI (Sociedad para la Investigación de Iones Pesados). La nueva instalación será organizada como un centro de investigación europeo/internacional, y estructurado como un Grupo Europeo de Interés Económico (EEIG, European Economical Interest Group).

En los últimos años, un amplio espectro de seminarios, grupos de trabajo, y comités internacionales han discutido y a la postre puesto las bases para el concepto de la nueva instalación. La estructura organizativa, el peso de las tareas científicas y el papel de cada miembro de la organización se discuten actualmente en grupos especializados, de los que la Universidad de Santiago de Compostela forma parte.

El objetivo principal de la nueva instalación es la construcción de un acelerador técnicamente innovador y único en el mundo que proveerá un extenso rango de haces de partículas [CDR01]. Se podrá contar con haces de protones y antiprotones y haces de iones de todos los elementos químicos hasta el uranio, que serán producidos con intensidades inéditas a nivel mundial.

Uno de los principales usos de los haces de iones de alta intensidad es la producción de haces energéticos de núcleos radioactivos de corta vida, en adelante referidos como Haces de Isótopos Singulares (RIB, Rare Isotope Beams). Los RIBs se producen en reacciones nucleares sufridas por los haces primarios de partículas estables. Por esta razón los científicos se refieren a ellos como haces secundarios. Para conseguir los haces secundarios de la intensidad deseada, la correspondiente intensidad de los haces primarios tiene que ser adecuadamente alta. El objetivo tecnológico del futuro sistema de aceleradores es llegar a multiplicar por un factor 100 las intensidades de los haces primarios respecto a las prestaciones actuales del GSI. Desarrollos tecnológicos paralelos serán necesarios para proveer detectores y equipo experimental adecuado. En este contexto el reto más importante es un avanzado sistema experimental que se llama “Reaction studies with Relativistic Radioactive ion Beams” ( $R^3B$ ) [R3B]. El conjunto experimental  $R^3B$  incluye, entre otras cosas, la realización de un espectrómetro magnético

superconductor (“Super Fragment Separator, Super-FRS) [SFRS] con una aceptación mucho mayor que el actual Fragment Separator (FRS) [FRS], que junta con las altas intensidades de los haces primarios, permitirán producir haces secundarios radioactivos con intensidades hasta 10000 veces más altas que las que se pueden conseguir hoy en día en el GSI.

Para conseguir las condiciones experimentales óptimas para una cierta investigación específica, la nueva instalación proveerá energías de haz hasta 15 veces más altas que las disponibles en el GSI para todos los iones, desde protones hasta uranio.

Obviamente, las altas energías e intensidades de los haces generan un problema desde el punto de vista ambiental y de seguridad, directamente relacionado con el alto índice de radioactividad producido. Se requiere una adecuada planificación del blindaje en torno a los aceleradores y áreas experimentales para asegurar que la radiación producida no escapará del área de confinamiento y que el nivel de radioactividad fuera de los laboratorios permanecerá por debajo del nivel natural de fondo.

Los RIBs se producen en reacciones nucleares inducidas por haces primarios de alta intensidad incidiendo en un blanco localizado a la entrada del Super-FRS. Además del haz secundario, que será transmitido a través del Super-FRS para su uso científico previsto, se producirán una gran cantidad de núcleos radioactivos de corta vida. La mayoría de ellos entrarán en el Super-FRS, serán desviados y abandonarán el Super-FRS lateralmente. Estos núcleos y las cascadas de neutrones que generarán tienen que ser parados en estructuras blindantes específicas. Para poder determinar la posición y el espesor de la estructura aislante, es necesario realizar una estimación fiable de la intensidad de los iones radioactivos producidos en las reacciones nucleares.

Este Trabajo de Investigación trata del estudio de la producción de núcleos radioactivos y de su propagación a través de Super-FRS. El medio para realizar el estudio ha sido el código Monte Carlo ABRABLA de simulación de reacciones nucleares, adecuadamente implementado para el propósito descrito anteriormente. Este trabajo ofrece una vista general sobre la producción de radioactividad en el área del Super-FRS, constituyendo el punto de partida para el diseño de la estructura blindante.

## Introduction

In February 2003, the German Federal Government approved the proposal for “An International Accelerator Facility for Beams of Ions and Antiprotons”. The future facility will be placed in Darmstadt, Germany, and represents an extension of the current GSI Laboratory (Gesellschaft für Schwerionenforschung). It will be organised as a European/international research centre, and structured as a European Economical Interest Group (EEIG).

In the last years a broad spectrum of workshops, working groups and international committees discussed and eventually set the basis of the facility concept. The organisational structure, the weight of the scientific tasks and the role of each member of the organisation are presently discussed in international task forces, to which also the Universidad de Santiago de Compostela takes part.

The principal goal of the new facility is the construction of a worldwide unique and technically innovative accelerator system that will provide an extensive range of particle beams [CDR01]. Proton and antiproton beams will be available and ion beams of all chemical elements up to uranium will be produced with world-record intensities.

The main employ of the high-intensity ion beams is the production of energetic beams of short-lived (radioactive) nuclei, in the following referred to as exotic or Rare Isotope Beams (RIBs). RIBs are produced in nuclear reactions experienced by the primary beams of stable particles. For this reason scientists refer to them as to “secondary beams”. To achieve the desired intense secondary beams, the primary beam intensities must be correspondingly high. Compared to the present GSI facility, a factor of 100 in primary beam intensities is the technical goal of the future system of accelerators. Technical developments are necessary also to provide adequate detectors and experimental set-ups. In this context, the most challenging item is the advanced experimental setup for “Reaction studies with Relativistic Radioactive ion Beams” ( $R^3B$ ) [R3B]. The  $R^3B$  experimental setup includes, among the other tasks, the realization of a super-conducting magnetic spectrometer (“Super FRagment Separator”, Super-FRS) [SFRS] with much larger acceptance than the present Fragment Separator (FRS) [FRS]. The large acceptance of the Super-

FRS, along with the high primary-beam intensities, would release secondary radioactive-beam intensities up to a factor 10000 higher than those currently achievable at GSI.

In order to meet the optimum experimental conditions for some specific investigation, the new facility will also provide beam energies a factor 15 higher than presently available at GSI, for all ions, from protons to uranium.

Obviously, the high energies and intensities of the beams open up the problem of the environmental and safety aspects, connected to the high rate of radioactivity produced. Adequate planning of the shielding around accelerators and experimental areas are required in order to assure that the produced radiation will not escape the confined area, and the level of radioactivity outside the laboratories will remain below the natural background level [Fes01].

RIB are produced in nuclear reactions induced by high-intensity primary beams impinging on a target placed at the entrance of the Super-FRS. Along with the secondary beam, which will be transmitted through the Super-FRS and then used for the designated scientific purpose, a large amount of short-lived nuclides (i.e. radioactive nuclei) are produced. Most of them will enter the Super-FRS, be bent, and then exit the Super-FRS from the sides. These nuclei, and the cascades of neutrons that they will generate, have to be stopped in devoted shielding structures. In order to determine the position and the thickness of the shielding, a reliable estimate of the intensities of the radioactive ions produced in nuclear reactions is needed.

In this “Trabajo de Investigación” we report on the study of the production of radioactive nuclides and of their propagation through the Super-FRS. The study was performed by means of a nuclear-reaction Monte-Carlo code, ABRABLA, opportunely implemented for the above-described purpose. This work offers an overview of the radioactivity production in the Super-FRS area; the latter is the required starting knowledge for the design of the shielding structure.

# Chapter 1

## The GSI Future Project

### *1.1 The GSI Future Project*

The proposed new facility consists of a 100/200 Tesla-meter double-ring synchrotron (SIS100/200) and a system of associated storage rings for beam collection, cooling, phase-space optimisation and experimentation (Figure 1.1) [Ang01]. It uses the present accelerators, the universal linear accelerator UNILAC and the heavy-ion synchrotron SIS18, as injector. Both synchrotron rings have the same circumference of about 1.1 km and will be installed underground in the same tunnel at a depth of 24 meters. All the other edifices, housing the Collector Ring (CR), the New Experimental Storage Ring (NESR), the High-Energy Storage Ring (HESR), the Super-conducting FRagment Separator (Super-FRS) and the experimental areas, will be build on ground. On-ground buildings will cover a surface approximately 14 hectare wide.

The project is based on many technological innovations. They will ensure world-unique characteristics, the most important of which are:

1) Full range of ion-beam species

The system of accelerators will accelerate all ions from protons up to the heaviest element, uranium. Beams of antiprotons with high intensity will be created from proton beams in the energy range of 1 GeV to 15 GeV.

2) High beam intensities

The 100 Tm synchrotron, SIS100, will produce intense pulsed ( $10^{12}$  ions/pulse) uranium ( $q = 28^+$ ) beams at 1.5 GeV/u and intense pulsed ( $2.5 \cdot 10^{13}$  ions/pulse) proton beams at 29 GeV. For the high-intensity proton beams an additional dedicated linac injecting into SIS18 is planned.

3) High beam energies

The 200 Tm synchrotron, SIS200, will provide high-energy ion beams with maximum energies around 30 GeV/u for  $\text{Ne}^{10+}$  beams and close to 23 GeV/u for fully stripped  $\text{U}^{92+}$  beams, respectively. The maximum intensities that are possible in this mode are  $5 \cdot 10^{10}$  ions per second.

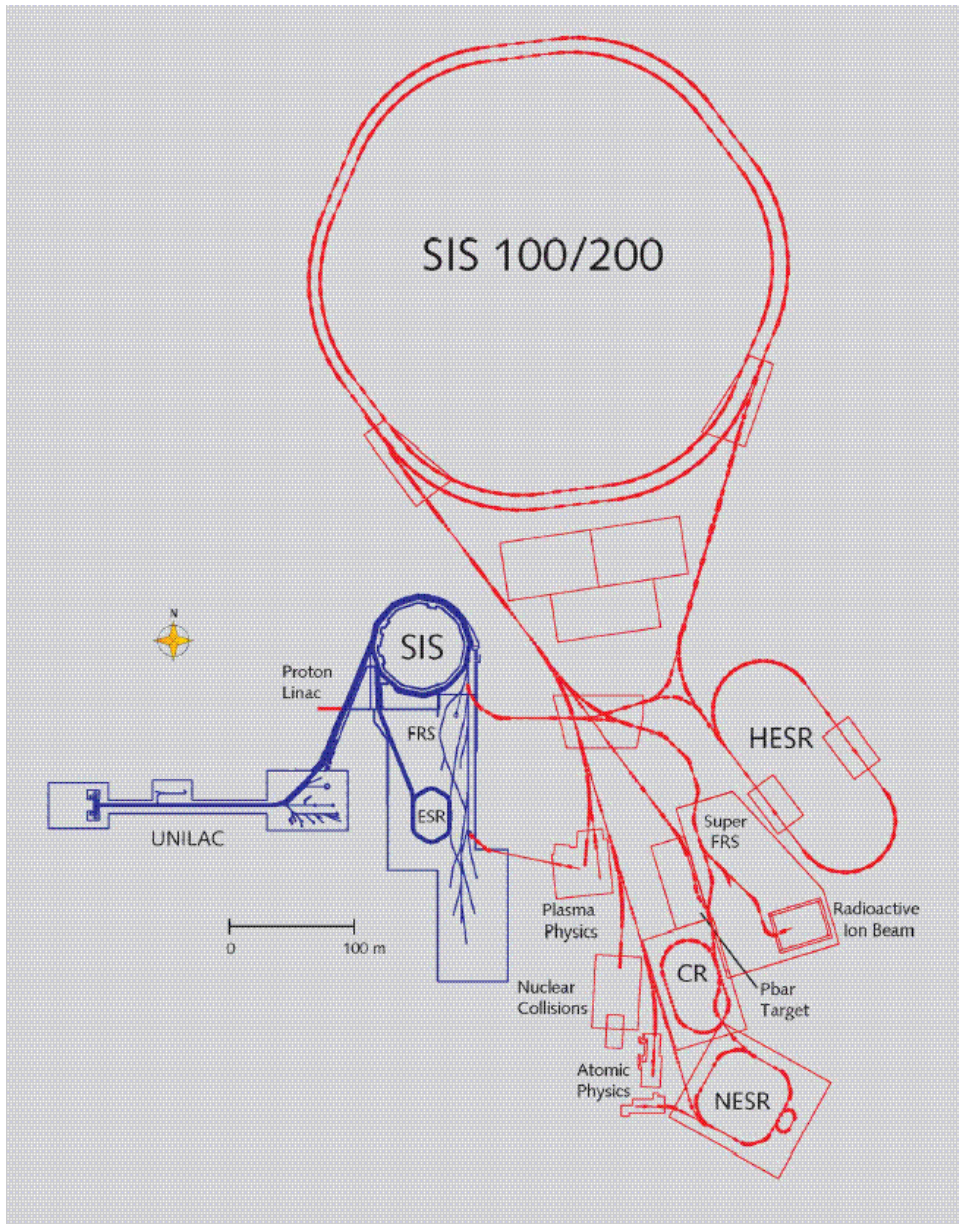


*Figure 1.1: Present layout of the existing UNILAC/SIS18/ESR facility (blue) and the planned new facilities (red): the Super-conducting Synchrotrons SIS100/200, the Collector Ring CR, the New Experimental Storage Ring NESR, the Super-conducting Fragment Separator Super-FRS, the proton linac, and the High-Energy Storage Ring HESR. The drawing also shows the planned experimental areas for plasma physics, nuclear collisions, rare ion beams, and atomic physics.*

4) High beam power

Short, high-intensity ion bunches will be available (both heavy-ion and proton beams can be compressed into 50 ns bunches). Ion pulses with a power of a thousand billion watts can be generated.

5) Parallel operation

One of the basic advantages of the double-ring concept is its ability to operate in parallel up to four different beams. This will be achieved by well-coordinated use of the accelerators and storage rings.

6) Slow extraction

High-energy beams can be extracted over extended periods (order of 10–100 seconds) as an essentially continuous beam. The slow extraction from the SIS100 is an additional option for extending the flexibility of parallel operation of experiments.

7) Brilliant beam quality

A collector ring (CR) will be used for stochastic cooling of secondary beams. This will produce ion and antiproton beams of extreme energy sharpness.

8) Storage rings

The “new experimental storage ring” (NESR) and the “high-energy storage ring” (HESR) will be used as accumulators and storage rings both for radioactive ions and antiprotons. Both rings will be equipped with stochastic and electron cooling devices to correct the beam degradation due to the interaction with the target.

9) Super-conducting Fragment Separator

With the Super-FRS magnetic spectrometer high secondary-beam intensities will be achieved. It will provide high-luminosity antiproton beams, high-energy proton and ion beams, and short ion pulses with energies up to 100 kJ.

The technical characteristics listed above will make experimentally accessible a wide spectrum of scientific scenarios. These are respectively:

1) Multi-disciplinary research

The full range of ion-beam species available at the new facilities will provide a broad basis for multi-disciplinary research. Investigation of quark matter, of hadronic matter, of hadron structure, of nuclear structure, of dense plasma, of atomic physics, as well as other interdisciplinary activities – like material research – will be performed at the new GSI facility.

2) Access to new types of secondary beams

Intensities of primary heavy-ion beams will increase by a factor 100. A wide bunch of new exotic nuclei will be produced and the corresponding secondary exotic beams exploited for the investigation of nuclear structure, astrophysics and for the study of fundamental interactions.

3) Compressed nuclear matter, charm production and antiproton beams

Nucleus-nucleus collisions at high beam energies will allow producing highly compressed nuclear matter. Studying highly compressed nuclear matter, physicists can reproduce the conditions that existed at the birth of the universe. Such extreme forms of matter may also exist at the centre of neutron stars. Collisions at high energies lead also to a maximum production rate of hadrons with strange quarks. This enables the study of charm production. At sufficiently high energies the threshold for the production of antiprotons is overcome. As a consequence, the production of intense antiproton beams will be possible.

4) Plasma physics experiments

The possibility to compress the ion beam into short bunches is indispensable for plasma-physics experiments. The knowledge of the behaviour of matter in the high-density plasma state is essential for inertial confinement fusion, and also for astrophysical studies.

5) Contemporaneity of four different scientific programs

The system of accelerators can operate in parallel up to four different beams. These are for instance: an antiproton beam, an exotic secondary beam, a high-energy heavy-ion beam (slowly extracted) for nuclear-collision experiments; intense beam pulses (with low repetition rates) for plasma physics.

6) Nucleus-nucleus collision experiments

The almost continuous beam – obtainable with the slow-extraction option – maximizes the luminosity in nucleus-nucleus collision experiments.

7) “Precision” experiments

Precision ion and antiproton beams will be achieved through sophisticated beam-handling methods, such as stochastic and electron cooling. Together with the statistical precision and high sensitivity that results from high beam intensities and interaction rates, the sharp-energy beams will allow to perform “precision” experiments, as for instance to determine the mass of short-lived, unstable nuclei, or to look for new particles associated with the strong interaction.

8) Mass measurements, electron-nucleus scattering and other research topics

The accelerator rings are unique in their capability to store, cool, bunch, and stretch beams and thus to fulfil the strict beam phase-space requirements from several experiments. Precision

mass measurements, electron-nucleus scattering and other research topics are accessible with the three rings.

9) Research with high-intensity secondary beams

The Super-FRS magnetic spectrometer will increase up to a factor 10000 the intensity of the radioactive-beam intensities with respect to the present GSI facility. This will allow to push the sensitivity of experiments involving short-lived nuclei and antiproton beams, which are the basis of much of the new research frontiers that will be explored in the new facility.

The facility is expected to serve about 2000 international scientists. About 140 new staff positions will be created for engineering, on-line testing and project management. The present estimate of the total cost of the facility is 675 million Euros. The proposed schedule for realizing the facility extends over 9 years.

## ***1.2 Physical Goals***

In this section we will shortly describe the physical goals achievable at the new facility. They can be sorted into 5 groups.

### ***1.2.1 Research with Rare-Isotope Beams – Nuclei far from stability***

The availability of RIBs allows the exploration of the structure and dynamics of complex nuclei in regions far away from stability. As any other physical system under extreme conditions, nuclei, pushed to their limits in neutron or proton numbers, reveal new features that lead to new insights and understanding. The study of nuclei far from stability will permit the study of the following three areas of investigation [Aum01].

#### *Nuclear-structure studies*

On the chart of the nuclides two lines mark the limits of the nuclear existence: the neutron dripline, beyond which the nucleus decays spontaneously by neutron emission, and the proton dripline, beyond which the nucleus decays spontaneously by proton emission. The driplines are in most part still unknown. With RIBs, nuclei at the driplines can be accessed. The structure and dynamics of such loosely bound nuclei is very different from that of stable nuclei. Rather diffuse surface zones, so-called halos and skins, were observed in neutron-rich unstable isotopes. Among other features unique to such exotic nuclei, one expects to encounter novel types of shell

structures, new collective modes, new isospin pairing phases, possibly new decay modes, or regions of nuclei with special deformations and symmetries. Effects of nucleonic clustering should become more prominent, giving rise to unusual nuclear geometries.

In an atomic nucleus two fundamental forces – the strong and the electroweak interaction – play a dominant role. The strong force plays the most decisive role. It fundamentally acts between the quarks, but some of this action leaks out of the nucleon and generates the attractive, short-ranged nuclear force between the nucleons. This nuclear force is counteracted by the repulsive electromagnetic force between the protons. The weak force transmutes unstable atomic nuclei into others and ultimately into stable nuclei. Experimental results on nuclear structure will provide the adequate benchmark for the nuclear theoretical models, which, in turn, will provide information on these fundamental forces.

In addition to the exploration of the driplines with exotic nuclei, the production of hypernuclei – nuclei where some nucleons are replaced by hyperons, nucleons that contain a strange quark – give access to a new and almost unexplored face of the nucleus. Hyperons are not restricted in the population of nuclear states as neutrons and protons are. Antiproton beams at the proposed facility will allow efficient production of hypernuclei with more than one strange hadron. These exotic nuclei offer a variety of new and exciting perspectives in nuclear spectroscopy and for studying the forces among hyperons and nucleons.

#### *Nuclear Astrophysics*

All atomic nuclei in the universe beyond lithium have been and still are being created in stars. In various stellar environments this ‘nucleosynthesis’ proceeds via the formation of transient nuclei that decay into stable ones, either directly or after several intermediate steps. The remnants of these processes, dispersed from dying stars into the interstellar space, eventually contract and serve as the seeds for a new generation of stars and their companions, such as our sun and the earth. Based on key properties of unstable nuclei, nuclear astrophysics is seeking for a reliable description of the various kinds of stellar nucleosynthesis by which all elements beyond lithium have been and still are being created. One of its major aims is to understand the abundance of the elements in the universe. Some of the presumed scenarios of matter creation in stars are: nuclear fusion, e.g. in the sun; explosive rapid neutron capture (r-process) possibly occurring during the outbreak of supernovae of type II; rapid proton capture (rp-process) occurring in novae explosions of accreting white dwarfs, or in X-ray bursts emerging from accreting neutron stars. The remnants of a supernova might become a fast-rotating neutron star with degenerate, ultra-

dense nuclear matter. At present, in particular the explosive nucleosynthesis is to a large extent not yet understood, due to the lack of appropriate nuclear data.

#### *Fundamental interactions and symmetries*

The Standard Model of Elementary Particle Physics summarizes our present knowledge on the fundamental building blocks of matter – the quarks and the leptons – and their interactions via exchange particles (so-called gauge bosons). It describes the electromagnetic, the weak and the strong force, and the fundamental symmetries (or symmetry violations) underlying these forces. The Standard Model has withstood three decades of extensive experimental scrutiny. Despite its great success, most physicists are convinced that the Standard Model eventually needs to be replaced or at least extended. The reason is that it contains disturbingly many parameters whose numerical values cannot be derived from the theory itself, and also other aspects that seem quite unnatural. Therefore, many high-energy physics experiments are aimed to search for possible extensions of the Standard Model. Besides these investigations in particle physics, low-energy precision experiments in nuclear and atomic physics also show a unique discovery potential for this field. The major thrust of the nuclear-physics studies focuses on the weak interaction, in particular on precision experiments of the beta decay of specific exotic nuclei, emphasizing symmetry violation and the different interaction types of the weak force.

#### ***1.2.2 Research with Antiprotons – Hadron Spectroscopy and Hadronic Matter***

The basic theory of the strong interaction is the Quantum Chromodynamics (QCD). In the QCD theory the quarks interact with each other by exchanging particles, the gluons. At short-distance scales, much shorter than the size of a nucleon ( $\ll 10^{-15}$  m), the basic quark-gluon interaction is sufficiently weak and one can apply perturbation theory, a computational technique that yields very accurate results when the coupling strength is small. Many processes at high energies can quantitatively be described by perturbative QCD. The perturbative approach fails completely when the distance among quarks becomes comparable to the size of the nucleon. Under these conditions, the force among the quarks becomes so strong that they cannot be further separated, in contrast to the electromagnetic and gravitational forces, which fall off with increasing distance. This unusual behavior is related to the self-interaction of gluons: gluons do not only interact with quarks but also among themselves, leading to the formation of so-called gluonic flux tubes connecting the quarks. As a consequence, quarks have never been observed as free particles, they are confined within hadrons, complex particles made of 3 quarks (baryons) or a quark-antiquark pair (mesons). Baryons and mesons are the relevant degrees of freedom in our

environment. An important consequence of the gluon self-interaction is the existence of hadronic systems consisting only of gluons (glueballs) or bound systems of quark-antiquark pairs and gluons (hybrids). If the predicted existence of glueballs and hybrids would be proven experimentally, our understanding of hadronic matter would be strongly corroborated. Along with this, an important and obscure part of the origin of the universe would be clarified. In fact, in the evolution of the universe, some microseconds after the big bang, a coalescence of quarks to hadrons occurred, which was associated with the generation of mass.

In the new facility, the high-intensity antiproton beams will provide access to the heavier strange and charm quarks and to copious production of gluons. For the testing of the QCD theory the charmonium spectroscopy, i.e. the spectroscopy of mesons built of charmed quark-antiquark pairs, is of particular interest.

### ***1.2.3 Nucleus-nucleus collisions at high energy – Compressed Nuclear Matter***

In nucleus-nucleus collisions at high energy highly compressed nuclear matter can be formed for a short time span of less than  $10^{-22}$  seconds in the collision zone. The compression phase is followed by an explosive expansion phase where hundreds of particles are emitted. The traces of these particles can give information on the properties of the nuclear matter. Specifically, the planned experiments address some of the most fascinating and challenging problems of strong-interaction physics: the phenomenon of confinement (why are quarks not observed as individual particles?) and the origin of the mass of hadrons (why is a hadron – that is composed of light quarks – much heavier than the sum of the masses of its constituents?).

In addition to its relevance for understanding fundamental aspects of the strong interaction, experiments with heavy-ion collisions can bring information on various, and so far unexplored, phases of the matter. In the collision, a major fraction of the kinetic energy of the two nuclei is converted into heat. If the energy pumped in the collision zone is sufficiently large, the hadrons melt, and the constituents, the quarks and gluons, can move freely forming a new phase, the quark-gluon-plasma. The temperature at which this deconfinement occurs, i.e. at which hadrons are expected to dissolve forming quark-gluon plasma, is about 170 MeV. Physicists suspect that in the early universe, about one millisecond after the Big Bang, such a phase transition occurred in the opposite direction, i.e. from the quark-gluon plasma into hadronic matter. The phase transition can occur for different combinations of temperature and density. Of special interest is also the possible transition at rather low energy but for highly compressed nuclear matter. This form of matter might exist in the interior of neutron stars.

#### ***1.2.4 Ion-Beam and Laser-Beam Induced Plasmas – High Energy Density in Bulk Matter***

Another research area of the actual and future GSI facility is the electron-ion plasma. In the electron-ion plasma, the electrostatic forces that bind the electrons with the nuclei are overcome. This condition is met in a wide range of temperatures and densities. There are indeed numerous sites in the universe where plasma exists, e.g. at the sun surface, the sun core or the center of Jupiter.

There are several methods to produce plasma in the laboratory such as electrical discharges in a gas or laser irradiation of a sample. The use of intense heavy-ion beams is a rather new and extremely powerful method with unique characteristics. By irradiating a solid-state target, uniform large-volume plasmas can be produced. At the same time, the ion beams also provide excellent diagnostic methods to analyse the plasma properties.

A particularly interesting plasma region – the dense, strongly coupled plasma – is located at relatively low temperature and high density. The interiors of the giant planets Saturn or Jupiter are interesting examples for this dense plasma region. At the new facility, strongly coupled plasmas with densities close to those prevailing in the center of Jupiter can be investigated. On the other hand, the PHELIX laser (Petawatt High-Energy Laser for Ion Experiments), which is presently being installed at GSI, allows to explore plasmas at higher temperatures, but lower densities. PHELIX is a laser in the kJ regime with the option to produce ultra-short, high-intensity light pulses with a total power above 1 PW ( $10^{15}$  W). This laser will be able to produce a light pressure exceeding the pressure in the interior of the sun.

To create hot and dense plasmas in the laboratory, the combination of these two beams – pulsed heavy-ion and laser beams – will be used synergistically. This technique will facilitate novel beam-plasma interaction studies on the structure and properties of matter under extreme conditions of high energy density, similar to those existing deep inside stellar objects, with keV temperatures and more than 100 times solid-state density.

Moreover, these studies open up the fascinating possibility of investigating the basic physics aspects of inertial confinement fusion – for many scientists a process that may represent the future energy supply for humanity.

### ***1.2.5 Quantum Electrodynamics, Strong Fields, and Ion-Matter Interactions***

In relativistic, high-Z ion-atom collisions, extremely intense photon fields arise due to the high nuclear charges and to the extremely high velocities. For the heaviest ions, Quantum Electrodynamics (QED), the ‘standard model’ of electromagnetism and a basis of modern physics, will be probed near the critical field limit associated with the extreme conditions of high charge states and high velocities. The fields, present in highly relativistic collisions, are strong enough to produce particle-antiparticle pairs (e.g.  $e^+e^-$ ) directly out of the vacuum.

At high values of the relativistic Lorentz factor the electric and magnetic fields increase dramatically and are strongly deformed. In contrast to lower energies, where magnetic forces are generally of minor importance, they start here to equal the electric ones. This high-relativistic region could not be addressed in any detail up to now. In the new facility, in the strong field limit, the study of subtle higher-order effects for elementary interaction processes as well as tests of fundamental symmetries will be experimentally accessible. At the New Experimental Storage Ring (NESR) the electron-electron interaction will be studied at the new electron target by means of cooled heavy-ion beams, decelerated in special cases for improved sensitivity.

Finally, we want to quote the applications of the interaction process of relativistic heavy ions with matter. These are for instance the material research, the biophysics, and the cancer therapy.

In the interaction with biological systems like the cells of human tissue or with electronic devices like computer memories, heavy charged particles can cause severe damage. In biology, alterations in the genetic code may cause cancer or long-term mutations. In electronic devices, the production of locally high ionisation densities and free charges causes single-event upsets or a local damage in semiconductors. The radiation hardness of electronic modules and satellite components can be tested with heavy ions before they are launched into space.

### ***1.3 Safety Aspects for Design and Operation of the New Facility***

The safety aspects that have to be considered for the design and operation of the new facility can be divided in two categories: those connected to the ionising radiation produced (radiation and activation safety) and those connected to the operation and handling of electric and magnetic devices (industrial safety) [Fes01]. In this section we will speak briefly about the radiation risks only.

Ionising radiations, i.e. beams of particles that, interacting with material, ionise the atoms of the material, are dangerous for their capability to produce shower of secondary particles – especially neutrons – that cannot easily be stopped in the vicinity of where they were produced. Moreover, objects lodged in zones that are regularly exposed to intense flux of neutrons become active. Figure 1.2 shows the zones where a high level of neutron production and activation is expected.

The target area of the Super-FRS is among those with higher level of dose rate and activation. There, beams of heavy nuclei, like uranium, with extremely high intensities, impinge on heavy production targets, with the consequent generation of a great variety of ionising radiations and a high flux of neutrons and gamma rays. Therefore, the design of the shielding in the target area of the Super-FRS has to be studied with great care.

The design of the shielding can be divided in three steps. First, the nuclear reactions occurring in the collision of the beam with the target have to be modelled with great care in order to produce reliable quantitative predictions of the produced nuclides (i.e. of the ionising radiations arising from the collisions) and of their velocities. Then, the kinematical characteristics of the produced secondary particles have to be used to estimate what is transmitted along the Super-FRS, what remains in the target area, and what is dispersed at the sides of the SFRS dipoles. Finally, the dose has to be estimated, i.e. the deposition of energy in the surrounding matter has to be evaluated from the knowledge of the fluxes of ions. In this “trabajo de investigación” we will study the first two points. An additional important aspect for the evaluation of the radiation, not only in the Super-FRS target area but also in zones far from it, is the evaluation of the fluxes of neutrons produced in the nucleus-nucleus collisions and in the successive interactions of the ions with the matter. This aspect is investigated with devoted experimental and theoretical studies [Feh02].

It is important to point out that a reliable estimate of the intensities of the flux of secondary nuclides impinging on the dipoles of the Super-FRS is of great importance also for the correct functioning of the machine, since a high level of radiation could cause the quenching (i.e. the stop of the super-conducting properties) of the super-conducting magnets. In the long term, intense fluxes of particles are also the reason of the malfunctioning and/or breakdown of the magnets. The radiation damage that they cause depends not only on the type of particle impinging but also on its kinetic energy. Therefore, a good knowledge of the kinematical properties of the radiation produced in the SFRS area is of great importance for the correct running and stability of the machine. Please note that the contribution of the reaction mechanism to the total kinetic energy is

not negligible. For example, the kinetic energy of typical intermediate-mass fission fragments can differ from the beam kinetic energy of about 200 MeV/nucleon.

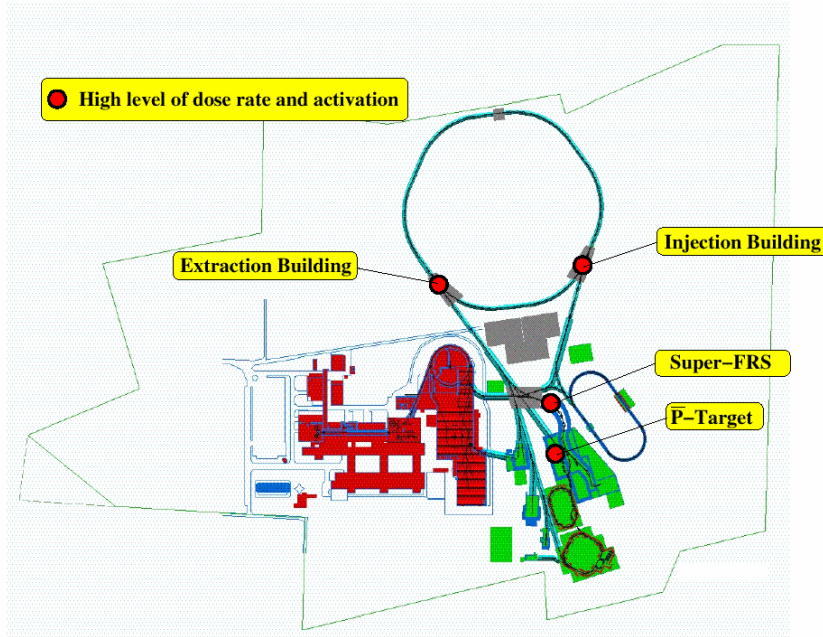


Figure 1.2: Overview of the new facility and position of the sites exposed to high neutron flux.

## Chapter 2

# The Superconducting Fragment Separator

In this chapter we want to present some features of the Super-FRS. The following description is not intended to be neither complete nor technically detailed. We will point out only those aspects that are relevant for the understanding of the work performed in this “trabajo de investigación”. In order to point out the basic characteristics of the Super-FRS, we will first shortly describe how its predecessor, the FRS, works. Therefore, at first we will recall some basic principles of the functioning of the FRS (section 2.1). Afterwards, in section 2.2, the Super-FRS will be described.

### 2.1 Basic principles of the Fragment Separator (FRS)

#### *Selection of a specific exotic beam with the FRS*

The FRS is a magnetic spectrometer composed of two sections (see Figure 2.1) separated by a layer of matter, acting as energy degrader [Gei92]. Each section contains two segments, composed of one dipole, five quadrupoles and two sextupoles. Before and after the dipole, two or three quadrupoles with a drift section in between acts as a lens for focalisation. That means that after focalisation nuclei with the same magnetic rigidities<sup>1)</sup> but different angles will fall on the same spot at the exit of the FRS. Sextupoles are used to correct for chromatic aberration, i.e. for the dependence of the position of the image on the kinetic energy of the particle.

The schematic behaviour of each section can be depicted as in Figure 2.2.

Two groups of particles with two magnetic rigidities,  $B\rho$  and  $B\rho'$ , that leave from point A will land on different x positions, B and C. The variation in position relative to the variation in

---

<sup>1)</sup> Inside the dipole the magnetic field,  $\vec{B}$ , is uniform and perpendicular to the velocity,  $\vec{v}$ , of the nucleus with charge  $q$  and mass  $m=m_0\gamma$ . Combining the 2<sup>nd</sup> law of dynamics and the Lorentz force, the circular trajectory of the nucleus respects the equation:

$$B\rho = \frac{m_0\gamma \cdot v}{q} = \frac{p}{q} \quad (2.1)$$

where  $\rho$  is the bending radius of the trajectory,  $p$  the momentum of the particle and  $\gamma$  the Lorentz factor. The ratio  $p/q$  ( $= B\rho$ ) is called magnetic rigidity and it is a characteristic of the particle with a certain mass, charge and velocity.

magnetic rigidity is a characteristic of the apparatus and it is called “dispersion”<sup>1)</sup>. If in the second magnet there is the same magnetic field as in the first one, for symmetry reasons two groups of particles with magnetic rigidities  $B\rho$  and  $B\rho'$  that leave from points B and C will land on the same position A'. In this working condition the spectrometer is therefore “achromatic”. The achromatism allows the image at the final focal plane to be independent of the momentum spread of the fragments at the entrance of the system<sup>2</sup>.

When the beam interacts with the target placed at the entrance, many nuclei are formed. Among all the produced nuclides we are interested in the selection and transmission of a specific nuclide, e.g.  $^{132}\text{Sn}$ . Due to the physics of the reaction mechanism  $^{132}\text{Sn}$  has a certain velocity distribution, which leads to a corresponding  $B\rho$ -distribution. The magnetic fields of the first two dipoles can be opportunely tuned so that most  $^{132}\text{Sn}$  nuclides transverse the FRS on the central trajectory. The distribution in magnetic rigidity of  $^{132}\text{Sn}$  will reflect in a distribution in x-position in the intermediate plane. Most of the  $^{132}\text{Sn}$  nuclides will arrive at the mid-plane (labelled “ $x_1$ ” in figure 2.2) in the central position, but the distribution will extend also towards B and C. Now, inserting opportune slits at  $x_1$ , so that there is a hole in correspondence to the central trajectory, one can stop particles with  $B\rho$  outside a certain range of x-positions, i.e. outside a certain range of magnetic rigidities. One can decide whether to cover great part of the  $B\rho$ -distribution of  $^{132}\text{Sn}$  (to maximise the intensity of the secondary beam) or just the central peak (to filter more). In both cases, there will be anyhow other fragments, those with magnetic rigidity inside the selected range, which may pass through the FRS along with  $^{132}\text{Sn}$ . Since the magnetic rigidity is a combination of A, Z and velocity, there is no possibility that the filter at  $x_1$  is enough to select  $^{132}\text{Sn}$ . For instance, light neutron rich fragments have the same A/Z of  $^{132}\text{Sn}$  and similar velocities. In addition, the velocity distributions of fragments with A/Z quite different from  $^{132}\text{Sn}$  can generate a  $B\rho$ -distribution that partially overlap with the  $B\rho$ -distribution of  $^{132}\text{Sn}$ .

A further selection criterion is needed.

---

<sup>1)</sup> The dispersion is defined as: 
$$D = \frac{dx}{dB\rho/B\rho} \quad (2.2)$$

<sup>2</sup> This device was originally introduced [Sim64] as “energy-loss spectrometer”, an apparatus used to study inelastic collisions with electron or ion beams with an energy resolution which is better than the energy spread of the primary beam. The energy-loss spectrometer is basically the scheme of figure 2.2, with the difference that a thin target is placed at the intermediate image plane instead of at the entrance. Some beam particles will interact inelastically, and either the projectile or the target nucleus will end up in an excited state. Since the target is thin and the electronic energy loss of the projectile is small, the system remains substantially achromatic. The x2-position is a measure of the energy lost by the projectile in the collision.



transmitted through the second section of the FRS. Inserting slits at the final image plane one can better purify the selected nuclide.

The two selection criteria are met by the fragments lying on the intersection of two lines on the chart of the nuclides, as for the example shown in figure 2.3 [Sch97]. The position of the first selection line depends on the magnetic rigidity set in the first section of the FRS. The position of the second selection line varies with the ratio of the magnetic rigidities of the 1<sup>st</sup> and 2<sup>nd</sup> sections of the FRS and with the thickness of the degrader. Due to the momentum acceptance of the FRS all the fragments in the overlap zone of the two hatched areas are transmitted. By setting the slits at the mid- and final planes one can reduce the extension of these areas. With this filtering it is possible to select a specific secondary beam and suppress most of the unwanted contaminants.

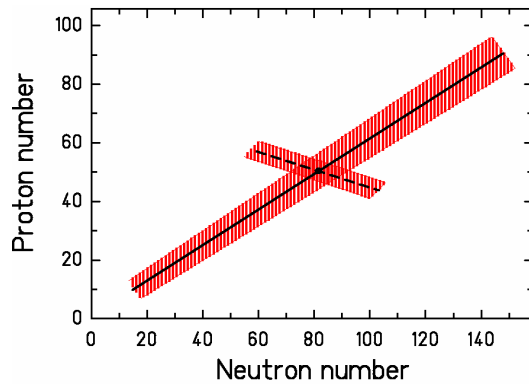


*Figure 2.3: Selection criteria, presented in the chart of the nuclides. Full line: first selection obtained tuning  $(B\rho)_{1st-section}$ . Dashed line: second selection obtained according to the ratio  $(B\rho)_{2nd-section}/(B\rho)_{1st-section}$  and choosing the degrader thickness. Roughly speaking, the first selection is a selection in  $A/Z$  and the second one in  $Z$ . Setting the slits at the intermediate and final planes one can reduce the hatched areas and in some favourable cases reduce them to a unique fragment ( $^{132}\text{Sn}$  in the example).*

It is clear that a pre-requisite for the correct spatial separation and filtering of the nuclei, both the beam and the produced nuclides have to be completely ionised, so that their effective nuclear charge,  $q$ , corresponds to their atomic number,  $Z$ . The stripping of the electrons occurs in the passage of the beam/fragments through layers of matter. Depending on the material of the layers and on the energy of the beam/fragments a certain charge-state population is reached.

To conclude, we want to enumerate here the characteristics necessary to produce secondary ion beams:

- High intensity of the primary beam. This is essential because most of the desired secondary beams are beams of exotic (i.e. rare) nuclei, whose production cross section are extremely low (from nanobarn to picobarn)

- High values of the transmission of the device. This is essential for the production of secondary neutron-rich nuclides originating in fission reactions. This aspect will be discussed again later.
- Selectivity of the apparatus. The ion-optical resolving power has to be high enough to separate ions of all masses. If the ions are well separated, using the slits at the intermediate and at the final planes, one can select the desired fragment.
- Sensitivity of the apparatus. There were experiments performed at the FRS where *one event* was sufficient to perform the desired investigation (this was the case for instance of a spectroscopy experiment of  $^{100}\text{Sn}$ ). Sensitivity, i.e. the capability to select even one single event, is essential for research with rare isotopes.

#### *The limited acceptance of the FRS*

One of the main constrains of the FRS is its limited momentum and angular acceptance.

The momentum acceptance of the FRS is limited to  $\pm 1\%$ . This means that if the magnets of the dipoles are tuned to the magnetic rigidity of 15 T·m, then only fragments within 14.85 T·m and 15.15 T·m will be transmitted through the FRS. All the other fragments will impinge on the iron wall of the dipole (see Figure 2.4). The limited momentum acceptance does not affect the

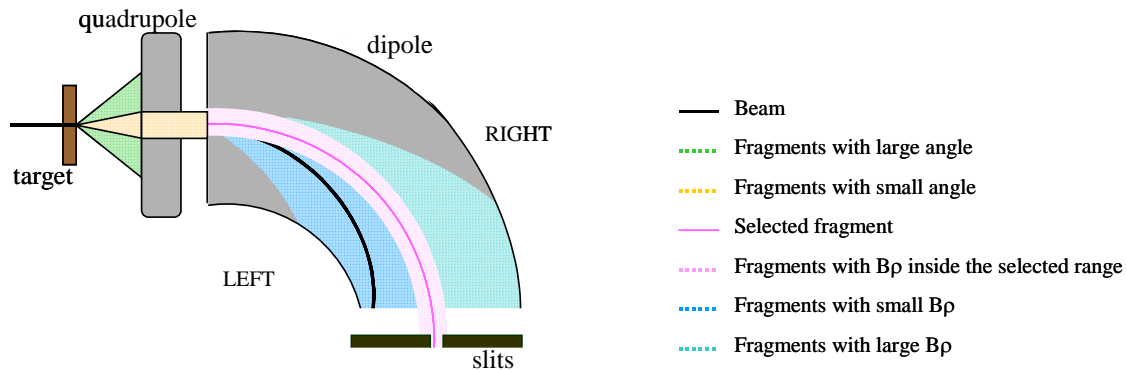


*Figure 2.4: Effects of the limited acceptance of the FRS. The beam impinges on the target and many fragments are generated in the nuclear reactions. Due to the high kinetic energy they are all going in forward direction. However, because of the limited angular acceptance many fragments do not enter the 1<sup>st</sup> dipole and are stopped in the walls of the 1<sup>st</sup> quadrupole. Due to the limited momentum acceptance, most of the fragments that enter the FRS are bent to the sides and impinge on the iron wall of the dipole. Only those with the selected magnetic rigidity can pass through the FRS.*

production of secondary beams (where a  $B\rho$  selection is made anyhow). It is not severe even for other kind of experiments where a complete overview of the production is desired; it is in fact possible to scan all the magnetic rigidities and then combine the results.

The limited angular acceptance is a bigger constraint. Because of it, not all the fragments that are produced are transmitted through the FRS. The restrictions brought by the limited angular acceptance (of about 15 mrad) are better understandable with the help of figure 2.5. The plot of the velocity of a residue is different depending on the reaction mechanism that produced it. In the case of fission, the produced nuclide feels the strong Coulomb repulsion of the fission partner. The magnitude of the velocity is determined basically by the charges of the two fission fragments. Since the process is isotropic, the resulting velocity is a shell in the centre-of-mass frame. In case of fragmentation, the Fermi momentum of the nucleons kicked out in the collision and the evaporation cascade of nucleons from the excited residual nucleus determine the velocity of the residual nucleus. In this case, the velocity pattern is represented by a full Gaussian distribution in the centre-of-mass frame. The larger is the number of removed and evaporated nucleons the larger the width of the Gaussian is. Therefore, for light fragmentation residues the full sphere of Figure 2.5 can become larger than the cone. The cone represents the limited angular acceptance of the FRS. What is actually transmitted through the FRS is what lies inside the cone. For heavy fragmentation products the transmission is about 100%, while for fission fragments it is about 5%.

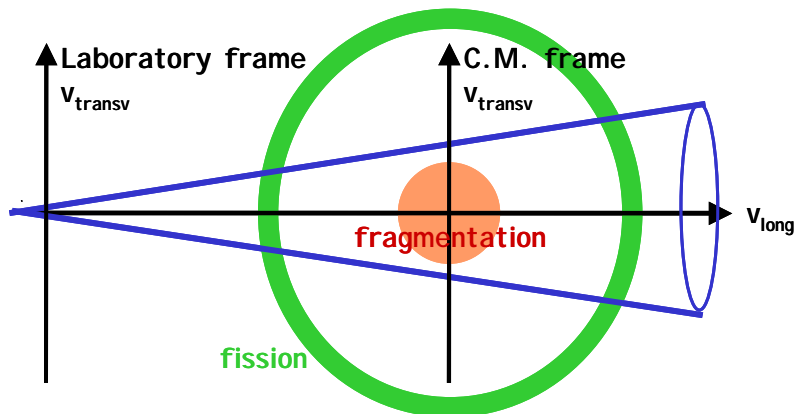


Figure 2.5: Pattern of the velocity in the centre-of-mass frame of a certain nuclide produced in fragmentation or in fission reactions. The cone represents the limited angular acceptance of the FRS. Only those products inside the cone are transmitted.

Originally the FRS was designed for the transmission and separation of heavy fragmentation residues. However, most neutron-rich exotic ion beams in the intermediate mass region are accessible preferentially via fission. In order to gain in intensity, the angular acceptance of the spectrometer has to be increased. This is the main reason why the Super-FRS will be built.

## 2.2 The Superconducting Fragment Separator (Super-FRS)

In the design of the Super-FRS [Gei03] the phase-space acceptance (i.e. angular and momentum acceptance) is increased drastically with respect to the FRS. The momentum acceptance is increased to  $\pm 2.5\%$ , the angular acceptance to 40 mrad in x direction and to 20 mrad in y direction. Though the acceptance is strongly increased, the ion-optical resolving power is preserved to guarantee the separation quality and the momentum resolution of the spectrometer, which is essential for the production of exotic nuclear beams. A comparison of the gain factors in transmission is illustrated in figure 2.6 for uranium fission products as a function of the atomic number. Of course, the transmission for the very light projectile fragments is also increased considerably. For example,  $^{19}\text{C}$ , produced in the fragmentation of  $^{40}\text{Ar}$  at 840 A·MeV, whose transmission is 22 % at the FRS, has a transmission of 71 % at the Super-FRS.

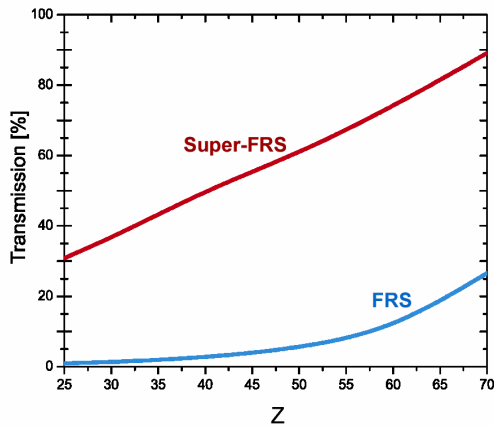


Figure 2.6: Comparison of the values of the transmission for uranium fission fragments with the Super-FRS and the FRS. The gain of pure transmission with the planned Super-FRS in the region of  $^{78}\text{Ni}$  is a factor of 30.

The separation method of the Super-FRS is in principle similar to that of the FRS, i.e., a two-fold magnetic deflection before and after a thick energy degrader. The combination of atomic energy loss and magnetic deflection provides spatially separated isotopic fragment beams.

However, special measures have to be applied due to the high phase-space acceptance and to the expected high intensity of the projectile beam. The higher phase-space acceptance creates large optical aberrations. Therefore, sextupole and octupole correction elements have to be implemented to achieve the necessary separation quality. The high primary-beam intensity leads to high production rates of parasitic fragments in the degrader, which may have comparable intensities of those produced at present in the target of the FRS. If these fragments were transmitted, they would eclipse the desired exotic nuclide. This problem can be solved by combining two separator stages, a pre-separator and a main-separator (see figure 2.7). Multiple separation stages are also efficient in reducing the background from the ionic charge states of the parasitic products.

Figure 2.7 gives an idea on how the Super-FRS works. The system consists of the pre-separator and the main separator, each equipped with an energy degrader. The pre- and main separators are independent achromatic systems, so the complete system is also achromatic. The quadrupole magnets are necessary to provide the ion-optical conditions at the different focal planes and optimize the operation of the dipole-magnets so to achieve the optimum resolution and transmission. The sextupole and octupole magnets are used to correct the image aberrations. The pre-separator (from F0 to F2) acts approximately like the FRS. Fragments are produced in the target, placed at the entrance (image plane F0). Many of them are deflected by the 1<sup>st</sup> dipole and exit the pre-separator. Those with the selected magnetic rigidities pass through and arrive at the first image plane F1 (first selection of figure 2.3). Due to the large momentum acceptance of the Super-FRS the amount of fragments arriving at F1 is still large. This can be seen in the first chart of the nuclides of figure 2.7. By appropriate tuning of the magnetic field of the second dipole and choosing an appropriate degrader, one can operate the second selection of figure 2.3 (see 2<sup>nd</sup> chart of the nuclides of figure 2.7). Using some slits, a bunch of fragments is selected. After the degrader at F4 there is a reduction in magnetic rigidity that depends mostly on the charge of the fragments. Seen on the chart of the nuclide, the second part of the separator selects the nuclei of a transversal band (the almost-horizontal hatched area of figure 2.3). Due to the lower energy of the fragments after the degrader at F4, the selected band is turned clockwise (see 3<sup>rd</sup> chart of the nuclides of figure 2.7). Different fragments follow different paths in the last section of the main separator. They land at F6 on different positions, and therefore many of them can be stopped in the slits. Because of the characteristics of the fission process, the band of parasitic fragments at F1 is quite large compared to fragmentation reactions. As a consequence, also at F6 the number

of remaining parasitic fragments is high. The remaining contamination can be eliminated using event-by-event tracking combined with time-of-flight and energy-loss measurements.

Another difference between the Super-FRS and the FRS concerns the target. The target at Super-FRS will be loaded with extremely high power, due to the high intensity of the beam. This requires special construction techniques (e.g., a rotating wheel). However, here we want to comment only about its thickness. Devoted studies have shown that the optimal target thickness ranges from few  $\text{g/cm}^2$  up to  $10 \text{ g/cm}^2$ , depending on the atomic number and on the energy of the beam. Thick targets bombarded with intense ion beams must face the highly focussed beam and therefore be able to dissipate large quantities of heat. In this context, it was shown that the most appropriate target materials are carbon and tantalum. For these reasons, in this work the calculations will be performed assuming the use of carbon and tantalum thick targets.

An essential input parameter in the calculation is the kinetic energy of the beam. The conclusion from devoted studies for the optimisation of the working conditions of the Super-FRS and the experience with FRS experiments show that the Super-FRS should accept beams up to a maximum magnetic rigidity of  $20 \text{ Tm}$  corresponding to about  $1.5 \text{ A GeV } ^{238}\text{U}^{92+}$ . This would represent the limiting case in our simulations.

Finally, we want to point out that the functioning of the Super-FRS requires new and challenging magnets. The requested large acceptance implies larger apertures of the magnets, and consequently larger fields. This can be achieved in a cost-effective way using superconducting magnets. Superconducting magnets are extremely sensitive to radiation. Long-standing radiation spoils the functioning of the device and has to be estimated for the scheduling of the maintenance of the facility. The radiation damage depends on the type of particles and on their velocity. Therefore, the implementation of a computational code capable to correctly estimate the production of radiation and its kinematical characteristics is essential. A second and more important aspect is that an intense and localised flux of radiation on the electric wires around the iron of the superconducting dipoles can cause the quenching of the magnet. Also in this case, the use of a computational code is essential for the correct design of the device.

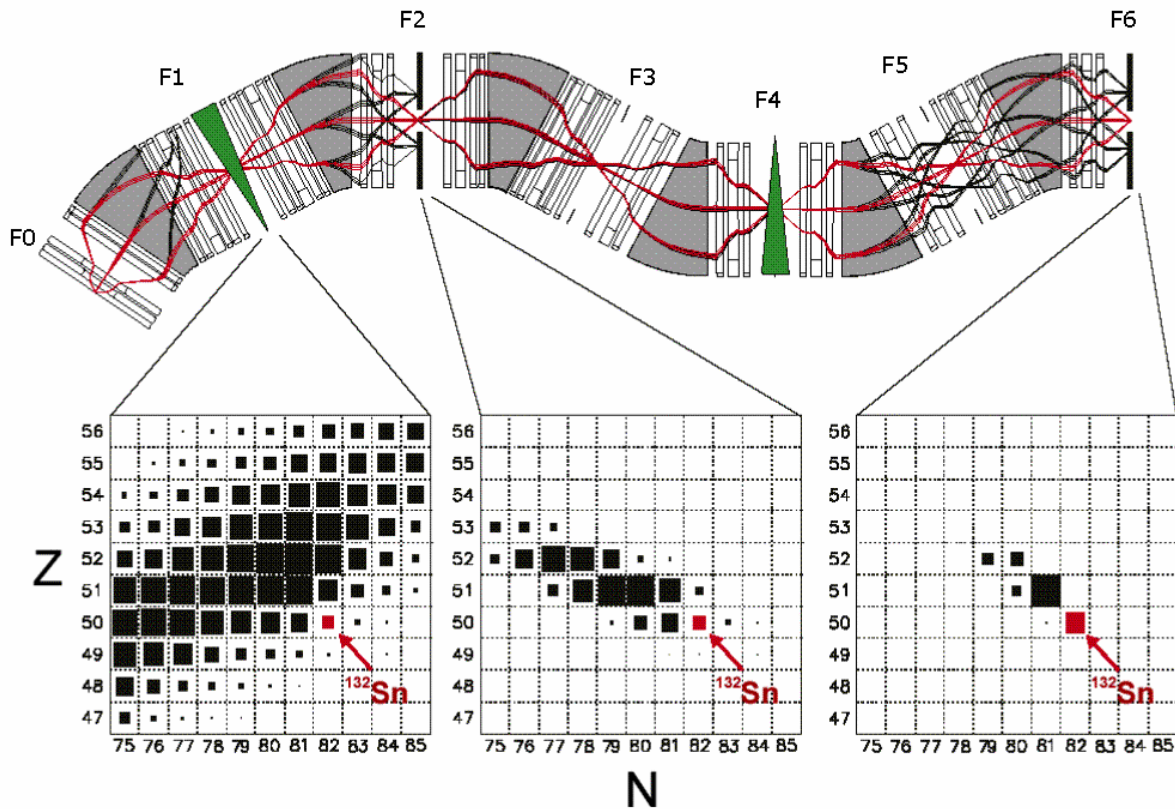


Figure 2.7: Separation principle of the Super-FRS consisting of the pre- and main-separator stage. In the presented calculated example a 1.5 A GeV  $^{238}\text{U}$  primary beam is focused on a  $4\text{ g/cm}^2$  carbon target with the goal to provide spatially separated  $^{132}\text{Sn}$  isotopes produced in the fission of uranium. The separation performance is illustrated by a presentation of the isotopes transmitted at different focal planes of the Super-FRS. The area of the isotopes in the N-Z plane represents the corresponding intensities resulting from transmission and production probability. The estimated production was calculated with the code MOCADI [Iwa97].

## Chapter 3

# Implementation of the ABRABLA code for the estimation of the RIB intensities at the Super-FRS entrance

### *3.1 Introduction*

The evaluation of the potential radioactivity in the Super-FRS target area requires employing computational programs capable to describe the nucleus-nucleus collision at relativistic energies with high predictive power. Three main types of approaches can be taken: an abrasion-ablation calculation, a microscopic calculation, and a quantum-mechanical calculation.

Abrasion-ablation statistical models can rather well describe nucleus-nucleus collisions at relativistic energies. In these models, the nuclei are considered as quasi-classical systems. Their fermionic nature is taken into account in an approximate way. Microscopic calculations (intra-nuclear-cascade codes or transport codes) are not suited for radioprotection purposes, since they take far too much computing time. In addition, their results are not very different from those of the abrasion-ablation model. More elaborate calculations, using a quantum-mechanic formalism (e.g. Fermionic nuclear dynamics [Fel00]), are just being developed and not yet applicable to large systems.

In the following sections, we will describe how the nucleus-nucleus interaction at relativistic energies is described in ABRABLA [Gai91, Ben98, Dej98, Jun98], the program that was used in this work to evaluate the intensities of the radioactive residues produced at the Super-FRS entrance. The ABRABLA code is a Monte-Carlo program that simulates the nucleus-nucleus collisions at relativistic energies according to an abrasion-ablation model. ABRABLA is continuously being developed at the GSI since the last 10 years.

The abrasion-ablation model is based on the idea that the nucleus-nucleus interaction can be schematized by the dynamical picture depicted in figure 3.1.

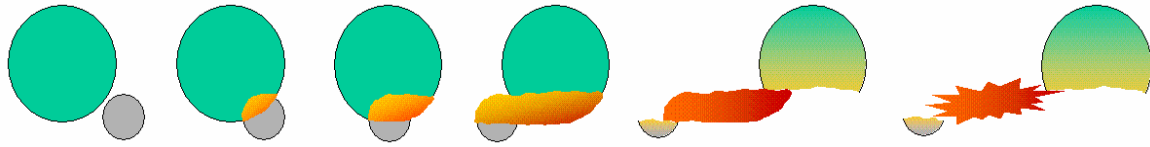


Figure 3.1: Schematic drawing of the nucleus-nucleus collision in the GeV energy regime.

The projectile nucleus and the target nucleus come into contact with some impact parameter. The two nuclei experience an “abrasion”, in which part of their mass is cut, like with a knife, according to their volumetric superposition. Only part of the nucleons of target and projectile are participating to the interaction. They are called “participants” and are filling the horizontal zone called “fireball” or “firestreak”. The parts of the projectile and target that do not participate to the interaction are called “projectile-spectator” and “target-spectator”, respectively. The projectile-spectator and the target-spectator acquire some excitation energy in the interaction. This excitation energy is consumed by a de-excitation process, called sometimes “ablation”, until the spectators reach a stable configuration, where they can only decay further by gamma emission. The de-excitation is described by the statistical model, where the evaporation of nucleons (and light nuclei, in some cases) and fission are competitive processes. Statistical considerations, connected to the number of available phase space for the nucleus, rule the probability of following one or the other channel. With the evaporation of one particle, the nucleus consumes some energy, but it can still be sufficiently excited to decay, and again fission and evaporation are competitive decay channels. If the nucleus fissions, the fission fragments usually have some excitation energy and can evaporate some nucleons.

The kinematical properties of the produced nuclides are very different depending on the reaction mechanism that generated them. These kinematical properties are not associable to the mass and charge of the fragment. In fact the same nuclide can be produced in different ways and arise from the collision with different kinetic energies and angles. For example, the nuclide  $^{42}\text{K}$  can be formed in the reaction  $^{238}\text{U}+\text{Ti}$  either by fission (figure 3.2 up) or by a long chain of evaporation of particles (figure 3.2 down). The number of protons and neutrons emitted, their velocity, their angular distribution, as well as the velocity and angular distribution of  $^{42}\text{K}$  are very different in the two cases. In the first case the Coulomb force between the two fission fragments confers an additional velocity in any direction of the space (since the process is isotropic). In the second case the fragment does not strongly modify its original velocity.

The nucleons participating to the fireball interact and move on the average in beam direction, according to a gradient that is zero for the nucleons close to target-spectator (at rest) and close to the projectile velocity for the nucleons close to projectile-spectator (moving with beam velocity). In addition, a transversal velocity has to be added, mostly due to the thermal expansion that the nucleons experience. All the binding energies are overcome, and no structure is preserved, with the result that all the protons and neutrons of the fireball will move very fast in all the direction of the space (but not isotropically in the laboratory frame).

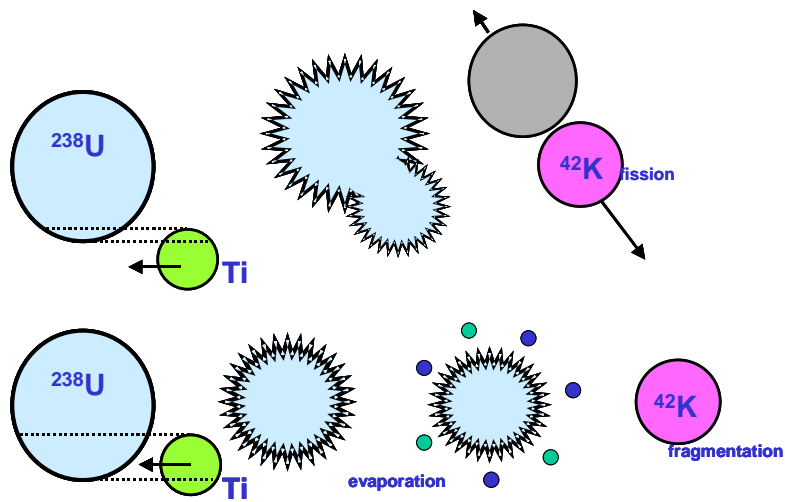


Figure 3.2: Example of the production of a certain nuclide (e.g.  $^{42}\text{K}$ ) in the collision of a  $^{238}\text{U}$  nucleus with a titanium nucleus. The nuclide can be produced either by fission reaction (up) or by fragmentation reaction (down). We observe the evolution of the  $^{238}\text{U}$ -spectator in the reference frame where  $^{238}\text{U}$  is at rest.

In this “trabajo de investigación” we implemented the kinematical description of the ions produced in high-energy nucleus-nucleus collisions in the ABRABLA code, as will be described in the following sections. The kinematical characteristics of the produced ions are of great importance to determine what is transmitted along the Super-FRS and what is bent and pushed aside. This is the basis for the geometrical mapping of the intensity of produced fragments in the Super-FRS entrance area.

### 3.2 The abrasion model in ABRABLA

In the description of the nucleus-nucleus collisions at relativistic energies, the first step is treated as an “abrasion” process [Gai91, Bro94]. At relativistic energies the bombarding energy is well above the Fermi energy. Under this condition, the interaction can be considered an ensemble of quasi-free nucleon-nucleon collisions. It is assumed that the trajectories of the interacting nucleons are straight lines and the nucleons participating to the interactions are those which belong to that part of the nucleus which geometrically overlap with the other nucleus. Therefore, the masses of the remaining nuclei (both projectile and target spectator) are determined by the geometrical overlap as function of the impact parameter. For a given projectile-target combination, the impact parameter determines only the number of removed nucleons from the initial nucleus, i.e. the abraded mass  $\Delta A$ , without specifying the proton-to-neutron ratio. The neutron number and the atomic number of the remaining nuclei are determined just by statistical consideration. The distribution of the N/Z-ratio after the collision can be calculated applying the hypergeometrical model. This model assumes that every nucleon removed has a statistical chance to be a neutron or a proton. This probability can be obtained with the combinatorial calculation. Assuming that the original nucleus had  $Z_{\text{initial}}$  atomic number,  $N_{\text{initial}}$  neutron number,  $A_{\text{initial}}$  mass number, and that  $\Delta A$  nucleons were removed, the probability,  $P(\Delta Z)$ , that  $\Delta Z$  protons were removed is given by:

$$P(\Delta Z) = \frac{C\left(\begin{matrix} Z_{\text{initial}} \\ \Delta Z \end{matrix}\right) \cdot C\left(\begin{matrix} N_{\text{initial}} \\ \Delta N \end{matrix}\right)}{C\left(\begin{matrix} A_{\text{initial}} \\ \Delta A \end{matrix}\right)} \quad (3.1)$$

$C\left(\begin{matrix} n \\ k \end{matrix}\right)$  is the binomial coefficient and gives the number of groups that can be formed taking out  $k$  objects of the total  $n$  objects. The hypergeometrical model corresponds to the extreme situation of no correlation at all between the nucleons during the abrasion phase, and results in the largest width obtainable for the distribution of the proton-to-neutron ratio. This implies that after the abrasion stage the remaining nucleus is left with a mean N/Z-ratio equal to its original N/Z-value, although with large statistical fluctuations, which lead to large variations in the N-over-Z ratio of the reaction products.

Before the collision, the nucleons occupying the overlapping volume of the two nuclei are distributed at random in momentum space inside the Fermi spheres of projectile and target in the Fermi-gas model (see figure 3.3). As they are removed they leave a “hole” to which is associated a certain energy. It is assumed that this internal energy of the single nucleons is redistributed among all the degrees of freedom of the remaining nucleus, which thermalises and forms a compound nucleus. The total excitation energy induced in the remaining nucleus is given by the sum of the hole-excitations with respect to the Fermi surface. Again, for statistical considerations, the mean excitation energy is proportional to the number of nucleons removed, i.e. to the abraded mass  $\Delta A$ . It was shown experimentally that for peripheral collisions the mean excitation energy gained per abraded nucleon is about 27 MeV [Sch93]. However, also the energy induced in the collision is subject to a large fluctuation and extends to rather high values. Therefore, the consecutive evaporation cascade has an important influence on the nuclear composition of the fragmentation products observed.

The same statistical approach is also used to determine the momentum distribution of the residual nuclei and their angular momentum. The momentum and the angular momentum of the fragment reflect the Fermi motion of the nucleons in the nucleus, and are directly connected to the nucleons that are kicked out of the nucleus during the abrasion stage. This part will be described in more details in section 3.4.

In conclusion, at the end of the abrasion stage, the surviving nucleus is characterised by 5 quantities: the mass, the charge, the excitation energy, the angular momentum, and the linear momentum. Only the first 4 affect the de-excitation process that will follow, and are used as input values for the “ablation” stage.

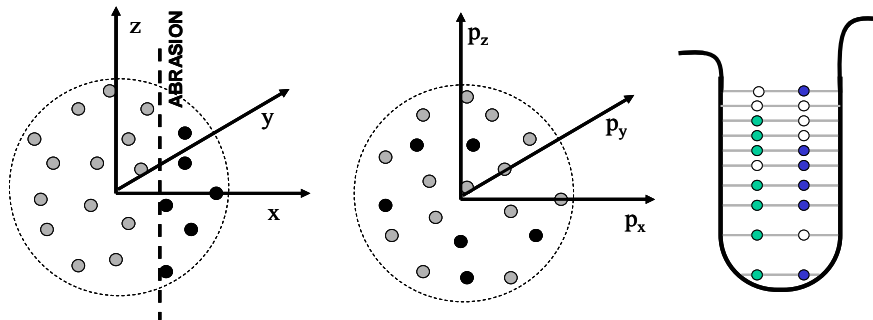


*Figure 3.3: Schematic picture demonstrating the action of the abrasion. The abrasion cuts away the nucleons occupying a well-defined area in space (left). These nucleons, however, are randomly distributed in momentum space (centre). As they are removed they leave a “hole” in the nuclear potential well, to which is associate a certain energy (right).*

### 3.3 The ablation model in ABRABLA

#### 3.3.1 The evaporation model

At the end of the abrasion stage the residual nucleus is supposed to be left in an equilibrium state, where the excitation energy acquired with the formation of a limited number of holes is now redistributed and shared by a large number of nucleons. This equilibrated system, called “compound nucleus” is characterized by its mass, charge, excitation energy and angular momentum, with no further memory of the steps that lead to its formation. The momentum of the nucleus does not affect the deexcitation process.

The excitation energy of the compound nucleus can be higher than the separation energy for neutrons, protons, alpha or light particles. So, all these particles can be emitted. Protons, neutrons and alpha constitute the most abundant part of the emitted particles, costing their emission a small amount of energy (in the order of few MeV). In the version of the ABRABLA code that was used in this work, the emission of heavier particles is neglected. The emission process can be well described as an evaporation from a hot system. The treatment starts from the formula of Weisskopf [Wei37], that is an application of the “detailed-balance principle”, which links the probabilities  $P_{i \rightarrow f}$  to go from a condition  $i$  to a condition  $f$  and vice versa ( $P_{f \rightarrow i}$ ) through the densities  $\rho_i$  and  $\rho_f$  of the states available in the two systems:

$$P_{i \rightarrow f} \cdot \rho_i = P_{f \rightarrow i} \cdot \rho_f \quad (3.2)$$

Weisskopf resolved the equation 3.2 for the specific case of particle evaporation. In that context,  $P_{i \rightarrow f}$  is the probability to evaporate a particle, i.e. to pass from the initial state of the compound nucleus (“mother nucleus”) to the final state of the daughter nucleus:  $P_{c \rightarrow d}$ . The inverse passage is represented by the fusion of the particle with the daughter nucleus and is ruled by the inverse cross section  $\sigma_{inv}$  – i.e. the cross section for the collision and capture of the particle – and by the characteristics of the particle. Consequently, the probability to evaporate a particle of type  $v$ , mass  $m_v$ , spin  $S_v \hbar$ , and kinetic energy  $E$  is given by:

$$P_{c \rightarrow d}(E) dE = \frac{(2S_v + 1)m_v}{\pi^2 \hbar^3} \sigma_{inv} \frac{\rho_d(E - E_v^{sep} - E_v^{bar})}{\rho_c(E)} dE \quad (3.3)$$

where  $E_v^{sep}$  and  $E_v^{bar}$  are the separation energy and an effective Coulomb barrier (that takes into account tunneling) respectively, and  $\rho_c$  and  $\rho_d$  are the level densities of the compound nucleus and the daughter nucleus, respectively. The total emission width  $\Gamma_v$  for the particle decay can be

found by integrating the equation between zero and the maximum possible eject energy. That gives:

$$\Gamma_v(E) = \frac{(2S_v + 1) m_v R^2}{\pi \rho_c(E) \hbar^2} T^2 \rho_d(E - E_v^{sep} - E_v^{bar}) \quad (3.4)$$

where  $R$  denotes the radius of the nucleus,  $T$  is the temperature of the residual nucleus after particle emission. In equation 3.4 was considered that the invariant cross section can be calculated geometrically knowing the radius of the nucleus. The thermodynamical relation between temperature and energy was used:  $E = a \cdot T^2$ , where  $a$  is the level-density parameter, typically equal to  $A/10$  MeV ( $A$ =mass of the nucleus). In ABRABLA the asymptotic level-density parameter  $\tilde{a}$ , as given in Ref. [Ign75], was used, that takes into account deviations from non-spherical nuclei. The density of excited states,  $\rho$ , is calculated with the well-known Fermi-gas formula [Hui72]:

$$\rho(E) = \frac{\sqrt{\pi}}{12} \frac{\exp(S)}{\tilde{a}^{1/4} E^{5/4}} \quad (3.5)$$

where  $S$  is the entropy calculated as described in reference [Gai91]. In ABRABLA there is no explicit dependence of the particle decay width on the angular momentum. This is because the fragmentation process at relativistic energies is expected to populate low angular momentum and therefore changes in angular momentum along the entire evaporation chain are negligible.

The emission probability of the particle of type  $v$  from the fragment with neutron number  $N$ , atomic number  $Z$ , and excitation energy  $E$  is given by:

$$W_v = \frac{\Gamma_v(N, Z, E)}{\sum_k \Gamma_k(N, Z, E)} \quad (3.6)$$

with  $k$  denoting all possible decay channels. The decay channels considered in the version of ABRABLA used in this work are: neutron emission, proton emission, alpha emission and fission.

### 3.3.2 The fission model

The evaporation process is in competition with another equilibrium process, that is fission. A fraction of the excitation energy may be spent to induce a collective deformation. As the shape of the nucleus departs from sphericity, the surface energy increases but the Coulomb energy decreases. The potential energy reaches a maximum at a deformation stage that is called ‘‘saddle point’’. The height of the potential energy over the ground state is the fission barrier  $B_f$ . Once a

nucleus reaches the saddle point, fission occurs and the nucleus separates into two complementary fragments.

Also for the fission probability the statistical method introduced before can be applied. Again, the level densities of the compound nucleus and the exit channel determine the probability. Here the exit channel is represented by the transition states in the fissioning nucleus in the saddle-point configuration, because this is a no-way-back configuration. In ABRABLA, the fission-decay width is calculated according to the transition-state-method of Bohr and Wheeler [Boh39], reformulated by Moretto [Mor75]:

$$\Gamma_{fiss}(E) = \frac{1}{2\pi\rho_c(E)} T_{fiss} \rho_{fiss}(E - E_{fb}) \quad (3.7)$$

where  $\rho_{fiss}$  is the level density of the transition states in the fissioning nucleus in the saddle point,  $E_{fb}$  is the fission barrier and  $T_{fiss}$  the corresponding temperature. The angular-momentum dependent fission barriers are taken from the finite-range liquid-drop model predictions of Sierk [Sie86]. In reality, the high excitation-energies induced in the relativistic nucleus-nucleus collisions performed at the GSI, require a special modeling of the fission decay width, which goes beyond equation 3.7. In this context, the evolution of the fission, determined by the interaction of the collective degree of freedom with the heat bath formed by the individual nucleons [Kra40, Gra83], is followed during the time. This modeling leads to a time-dependent fission width  $\Gamma_f(t)$ . A dominant parameter is the dissipation coefficient,  $\beta$ , which rules the influence of the nuclear viscosity on the time needed for the deformation. A comprehensive study and description of this treatment was recently done in ref. [Jur02].

Once fission occurs, the characteristics of the fission fragments have to be described. This is done in the fission code PROF1 [Ben98], used as subroutine of the ABRABLA code. PROF1 is a semi-empirical Monte-Carlo code developed to calculate the nuclide distributions of fission fragments. In the model, for a given excitation energy,  $E^*$ , the yield of the fission fragments with neutron number  $N$ ,  $Y(E^*, N)$ , is determined by the number of available transition states above the potential energy at the fission barrier. It is assumed that the mass-asymmetric degree of freedom at the fission barrier is on average uniquely related to the neutron number  $N$  of the fission fragments. The number of protons and neutrons are considered to be correlated (although small fluctuations in the charge density are also introduced in the model). The barrier as function of the mass asymmetry is defined by three components (or “channels”). The symmetric component, defined by the liquid-drop potential, is described by a parabola. Two other components, the

asymmetric ones, describe the neutron shells at  $N=82$  and around  $N=88$  (known in literature as “standard I” and “standard II”). They modulate the parabolic potential with four Gaussian functions. At high excitation energies, the effects of shells are not perceptible anymore, and only the parabolic potential is reflected in the mass distribution of the fragments. The excitation energies of the fragments are calculated from the excitation and deformation energy of the fissioning system at the scission point. A full description of the model is given in [Ben98].

### ***3.4 The kinematics of the nucleus-nucleus collision***

#### *Fragmentation residues*

Here we will discuss about the momentum distribution of the fragmentation residues in the context of projectile fragmentation. We will describe facts in the beam reference frame, i.e. in the frame where the projectile is at rest.

Fragmentation residues are those leftover after the abrasion and the successive chain of evaporation of particles.

In the frame of the Fermi-gas model, the momenta of the nucleons are distributed in a Fermi sphere. Their vectorial sum gives the momentum of the nucleus, which is zero in the centre-of-mass frame. Since the momenta of the ejected nucleons in the abrasion are sampled randomly from the distribution (see figure 3.3-center), for momentum conservation the surviving spectator will exhibit a Gaussian momentum distribution. Goldhaber [Gol74] calculated the width of this distribution and found that it is proportional to the square root of the abraded mass. Crespo et al. [Cre70] calculated the random combination of small recoil momenta from the sequential evaporation of nucleons and found that it contributes to the width of the momentum distribution of the residual fragment by a quantity proportional to the square root of the evaporated mass. Between the two contributions, the one originating in the abrasion stage is dominant.

Both in the abrasion and in the evaporation processes, the nucleons escaping can occupy any position in the momentum space. Therefore, the mean value of the distribution does not change, and the mean velocity of the fragmentation residue is the same as the velocity of the projectile, i.e. it is zero in the beam frame. In first approximation this conclusion is correct. To a more correct analysis, the mean velocity of the fragments is not zero, but it is modified in the component along the beam direction, the “longitudinal” component. The mean velocity of the fragmentation residues is influenced by two effects. The first effect is a kind of “friction”

phenomena that the nucleus experiences during the abrasion with the other nucleus. The net result, as demonstrated in ref. [Abu76], is a reduction of its longitudinal momentum, which becomes negative in the beam frame. In ref. [Abu76] it was shown that the reduction of the longitudinal momentum is proportional to the abraded mass  $\Delta A$ .

The effect of friction is overcome by another effect that comes into play at smaller impact parameters. In this case the collision is violent enough to generate a kind of explosion of the fireball that is in between the two spectators. This explosion causes an acceleration of the two spectators [Ric03].

In 1989 Morrissey [Mor89] derived semi-empirical parameterisations for the longitudinal momentum transfer (proportional to the abraded mass,  $\Delta A$ ) and for the width of the Gaussian distribution (proportional to the square root of the abraded mass,  $\sqrt{\Delta A}$ ). However, the validity of these parameterisations is restricted to peripheral collisions.

For this reason, we preferred not to use any parameterisation in ABRABLA and we estimated the momentum distribution of the prefragment after the abrasion, using Goldhaber's results. The effects due to friction, fireball blast, and evaporation are neglected because they are of minor entity.

The program calculates the standard deviation,  $\sigma$ , of the Gaussian momentum distribution of the prefragment after the abrasion according to Goldhaber's prescription [Gol74]:

$$\sigma = \sigma_0 \cdot \sqrt{\frac{A_{proj} (A_{proj} - A_{prefrag})}{A_{proj} - 1}} \quad (3.8)$$

where  $\sigma_0$  is given by  $p_{Fermi} / \sqrt{5}$  and it is approximately around 118 MeV/c for most of the prefragments.  $A_{proj}$  and  $A_{prefrag}$  indicate the mass of the projectile and that of the prefragment, respectively. The three components of the momentum of the prefragment are then randomly sampled from a Gaussian distribution with standard deviation  $\sigma$  and mean value 0. The velocity is then obtained dividing by the prefragment mass.

As commented above, the evaporation of particles does not affect sensitively the momentum distribution of the final fragment. However, it is interesting to consider the spectrum of the evaporated particles. Starting from equation 3.3, assuming the evaporation of a specific type of particle (e.g. neutrons), assuming that the inverse cross section is constant and introducing some simplification in the level densities of equation 3.5, one obtains the following energy distribution for the evaporated particles:

$$P_v(E)dE \approx E \cdot e^{-\frac{E}{T}} dE \quad (3.9)$$

from which the evaporative Maxwellian shape of the spectrum is evident. In the program, in each evaporative step, the energy of the prefragment is reduced by the particle separation energy, by the Coulomb barrier (when existing) and by the kinetic energy of the particle. The kinetic energy of the particle is randomly sampled from a Maxwell distribution, as in equation 3.9, defined by the temperature of the prefragment (the temperature is connected to the excitation energy by:  $E = a \cdot T^2$ , where  $a$  is the level density parameter). A typical value of the kinetic energy for evaporated neutrons is around 3 MeV, which is quite a low energy. The emission of protons is reduced and the spectrum is shifted toward higher energies due to the Coulomb barrier.

#### *Fission residues*

The kinematics of the fission process is treated inside the program PROFI [Ben98]. The mean velocity of fission fragments is estimated by the following empirical description of the total kinetic energy:

$$TKE = \frac{Z_1 Z_2 e^2}{D} \quad \text{with} \quad D = r_0 A_1^{1/3} \left( 1 + \frac{2\beta_1}{3} \right) + r_0 A_2^{1/3} \left( 1 + \frac{2\beta_2}{3} \right) + d \quad (3.10)$$

where  $A_1, A_2, Z_1, Z_2$  denote the mass and charge numbers of a pair of fission fragments prior to neutron evaporation.  $D$  represents the distance between the two charges and is given by the fragments radii ( $r_0 A^{1/3}$ ), corrected for the deformation ( $\beta$ ), plus the neck ( $d$ ). The parameters ( $r_0 = 1.16$  fm,  $d = 2.0$  fm,  $\beta_1 = \beta_2 = 0.625$ ) were deduced from experimental data in ref. [Böc97] and are consistent with values previously found in the analysis of ref. [Wil76]. At low energies, the dependence of the  $\beta$  parameters on the fission channel is considered. When the momentum conservation is imposed to the reaction, the velocities of the two fission fragments are determined.

### ***3.5 Limitations and applicability of the ABRABLA code for radioprotection purposes***

The output information given by ABRABLA after the implementation performed in this work is the Z, A and velocity of the residues from the projectile. This is sufficient to have a mapping of

the intensities of the secondary nuclei produced in the Super-FRS target area, which is the purpose of this work.

However, the modeling of the nucleus-nucleus collision realized in ABRABLA has some limitations, connected to the approximations used in the descriptions of the physical processes. The use of the code is therefore limited by the following conditions:

- target and projectile must have mass larger than 10
- the beam kinetic energy should be larger than about 100 MeV per nucleon
- the total energy of the system in the center of mass should be much larger than the sum of the binding energies of projectile and target

These limitations do not touch the cases studied here, which concerns heavy-ion interactions at relativistic energies.

A quite important restriction of the applicability of the ABRABLA code for radioprotection purposes is that its predictive power is limited to fragments above  $Z \cong 10$ . While the production of intermediate and heavy fragments can be successfully performed with the evaporation-fission mechanisms, as described in ABRABLA, most of the light fragments are produced with another reaction mechanisms: multifragmentation. Multifragmentation takes place when not-peripheral collisions occur. In these events, the simultaneous formation of several light ( $Z < 10$ ) fragments is occurring: the “multiplicity” – i.e. the number of produced fragments per event – is bigger than one. Although the probability that multifragmentation events occur is rather low, the high multiplicity contributes to increase noteworthy the intensity of the very light fragments. We will comment on this restriction in the next chapter.

Another restriction is that the model describes only the nucleus-nucleus interaction itself, i.e. the code works only for thin targets. In the calculations performed in this work, thick target were assumed. This introduces an error, which will be discussed in the next chapter.

A more detailed mapping of the radioactivity building up in the new facility requires information not fully provided by ABRABLA. These are for instance the neutron production in the reaction and their transport through the matter (with consequent secondary reactions) and the secondary reactions of the fragments in thick targets, which produce additional amounts of neutrons. The knowledge of the fluxes of neutrons produced in the new facility is a particularly important issue because it affects the planning for the construction of the shielding. Obviously, a comprehensive transport code would be more appropriate for this purpose. However, most of the transport codes for nuclear reactions do not treat nucleus–nucleus collisions, at least not for

medium-mass and heavy nuclei. Monte-Carlo codes as LAHET-MCNPX [LCS] are indeed more suited for the calculation of neutron fluxes in complex geometry, but, unfortunately, they only treat the case of nucleon-nucleus collisions. Recently, nucleus-nucleus collisions were implemented in FLUKA [FLU], GEANT [GEA] and SHIELD [SHI], but still the accuracy of the results have to be benchmarked. In fact, these transport codes suffer of some deficiencies, which reduce the accuracy of the result. Specifically, these codes were developed for the simulation of other physical cases, like high-energy particle interactions or low-energy neutron interactions. The treatment of the heavy-nuclei collision at energies around 1 GeV/nucleon is in some cases fragmentary. This is for instance the case of the fission mechanism, which is often parameterized. The consequence is that the predictive power for the production yield of the residual nuclei is often scarce. On the other hand, the total reaction rate and the evaluation of the neutron fluxes and angular distributions are rather realistic.

For the design of the shielding around the Super-FRS and for the handling of the Super-FRS itself, a good knowledge of the secondary beam production is essential. In fact, if the  $A/Z$  of the most produced isotopes is wrongly estimated, due to the bending occurring inside the dipoles, also the radiation arriving at the iron walls of the spectrometers is wrongly estimated.

A correct mapping of the secondary beams impinging on the iron walls of the dipoles and on the concrete shielding relies upon an accurate estimate of the yield of residues and on their velocity. This justifies the work performed with ABRABLA. ABRABLA was extensively benchmarked and its predictive power widely tested. It provides results that are in excellent agreement with the experimental data. For many reactions, the formation cross sections of the most produced isotopes are predicted with few percent relative error, and the most exotic nuclei with few tens of percent of relative error. The other codes available are often off of even 3 orders of magnitude.

## Chapter 4

### Results and discussion

Once the production of the fragments is simulated with ABRABLA and the production cross sections estimated, the transport of the fragments along the Super-FRS has to be done. To this purpose we wrote an analysis program. The program was written in PL/I [PLI]. The SATAN [SAT] graphic package was used to set the gate conditions and for the graphic presentations.

#### *4.1 Analysis of the data*

##### *The analysis program*

The output of the ABRABLA simulation gives event-by-event the following quantities:

- the mass number of the final fragment
- the atomic number of the final fragment
- the x, y, and z components of the velocity of the fragment in the beam frame

and other additional information like the impact parameter, the number of abraded neutrons and protons, the number of evaporated neutrons, protons and alpha particles, the type of reaction (nuclear reaction without fission; electromagnetic excitation – i.e. coulomb interaction without collision – without fission; electromagnetic excitation with fission; nuclear reaction with fission), the energy of the prefragment after abrasion, the energy at fission (above the fission barrier).

The three quantities listed above are those used to draw the map of the produced nuclides in the Super-FRS target area.

The simulation gives the results for a nucleus-nucleus collision, i.e. for the case of an infinitely thin target. The feasible experimental cases for the future Super-FRS facility assume the use of rather thick production targets. In addition to the target, another layer of matter, the stripping foil, has to be traversed by beam and fragments. The passage through these two layers of matter has two consequences: the first is that both the beam and the fragments experience some energy loss and consequently reduce their velocity; the second is that the fragments themselves can interact with the target/stripper nuclei, i.e. perform secondary reactions. In this analysis we

will take into account only the first case and neglect the second one. The first case has to be considered because a correct evaluation of the velocity of the beam/fragment is essential for the correct knowledge of its magnetic rigidity, and, consequently, of its bending inside the dipoles of the spectrometer. Therefore, for a reliable mapping of the intensities of the nuclides produced, a correct knowledge of the velocity is essential. On the contrary, secondary reactions can be ignored. In fact their effect is to reduce the production of a given nuclide of a few percent, and increase the production of other nuclides. A variation of a few percent does not change the order of magnitude of the intensities, whose knowledge is the purpose of this work.

Let us consider how the reduction of velocity occurs. A beam exits from the synchrotron with the energy per nucleon of 1.5 GeV, corresponding to the velocity in the laboratory frame  $v_{beam-init} = 26.69$  cm/ns. The energy in the synchrotron, measured by determining the revolution frequency, is taken as a reference. The velocity of the reaction products in the laboratory frame has to be calculated considering three contributions:

- 1) The energy loss of the beam. Before the nuclear reaction occurs, the beam transverses some layers and part of the target and reduces its energy because of Coulomb interactions with the electrons of these materials. So at the moment of the reaction, the velocity of the beam –  $v_{beam-react}$  – is reduced with respect to the initial one. The value of  $v_{beam-react}$  is calculated with the following passages: 1) the range of the beam in the target is calculated considering the initial beam energy, its mass, its charge and the mass and charge of the target; 2) the position (depth) in the target at which the reaction occurs is chosen randomly (with equal probability for every point) and the thickness of the two sections<sup>1</sup> of the target is calculated; to these thickness correspond a range; 3) the range of the beam is reduced by the thickness of the first section of the target; 4) the reduced range of the beam is transformed back into energy and the energy into the velocity in the laboratory frame. All these passages were performed using some procedures taken from ref. [Röh94].
- 2) The nuclear reaction releases a certain velocity to the fragment. This velocity is the output data of ABRABLA, given in the beam frame. It is transformed into the laboratory-frame velocity by means of the Lorentz transformations:

$$\beta = \frac{v_{beam-react}}{c} \quad (4.1)$$

---

<sup>1</sup> The sections behind and beyond the point where the reaction occurs.

$$\begin{aligned} v_x^{lab} &= \frac{v_x \cdot \sqrt{1-\beta^2}}{1 - \frac{\beta v_z}{c^2}} & v_y^{lab} &= \frac{v_y \cdot \sqrt{1-\beta^2}}{1 - \frac{\beta v_z}{c^2}} & v_x^{lab} &= \frac{v_z + v_{beam-react}}{1 - \frac{\beta v_z}{c^2}} \end{aligned} \quad (4.2)$$

where  $-v_{beam-react}$  is the velocity with which the laboratory frame is moving with respect to the beam frame,  $c$  is the velocity of the light,  $v_x, v_y, v_z$ , are the components of the velocity of the fragments in the beam frame, and  $v_x^{lab}, v_y^{lab}, v_z^{lab}$  are the components of the velocity of the fragments in the laboratory frame. The component along the beam direction is conventionally the z-axis. Please note that the relative velocity between the two systems is  $v_{beam-react}$ .

- 3) Finally, the fragment has to transverse part of the target and the stripper, depositing in them some energy and reducing consequently its velocity. Again, to calculate the reduction of its velocity the following passages are done: 1) the energy of the fragment is calculated from its velocity; 2) the range of the fragment in the target is calculated considering its energy, its mass, its charge and the mass and charge of the target; 3) the range of the fragment is reduced by the thickness of the second section of the target; 4) points 2 and 3 are redone for the case of the stripper; 5) the reduced range of the fragment is transformed back into energy and the energy into the velocity in the laboratory frame. We label this velocity with  $v_x^{lab}$ ,  $v_y^{lab}$ ,  $v_z^{lab-reduced}$ . All these passages were performed again using the procedures taken from ref. [Röh94].

The velocity with which the two reference frames are moving is calculated considering the point where the fragment is generated, i.e., where the nuclear reaction occurs. The production of fragments in the stripping foil is neglected because the mass of the foil is about 2% the mass of the target.

Having done the procedures described above, we have the velocity of the fragment in the laboratory frame after the passages through the layers of matter. Please note that we assume that the passage through the matter, and the consequent energy loss  $\Delta E$ , changes the  $B\rho$  of the fragment but does not affect the angle  $\theta$ . With this information we can calculate the orthogonal velocity  $v_{\perp}^{lab}$ , the angle  $\theta$ , and the magnetic rigidity  $B\rho$  of the fragment:

$$v_{\perp}^{lab} = \sqrt{(v_x^{lab})^2 + (v_y^{lab})^2} \quad (4.3)$$

$$\theta = \arctan\left(\frac{v_{\perp}^{lab}}{v_z^{lab-reduced}}\right) \quad (4.4)$$

$$B\rho = \frac{u}{e} \frac{A}{Z} \beta \gamma c \quad (4.5)$$

where  $A$  is the mass number,  $Z$  is the atomic number,  $u$  is the atomic mass unit,  $-e$  is the electron charge,  $\gamma = (1 - \beta^2)^{-1/2}$ .

### *Analysis of the results*

Making this procedure for every event, the spectra presented in figure 4.1 could be filled. Figure 4.1-left presents the acceptance plot of all fragments produced in some nuclear reaction (in the example, a  $^{238}\text{U}$  beam at 1.5 GeV per nucleon impinging on an infinitely thin tantalum target). This two-dimensional spectrum collects the number of fragments (coloured pixels) having a certain magnetic rigidity (x-axis) and produced with a certain angle (y-axis). In this plot, the position of the beam is represented by a spot, whose coordinates are  $x = 16.64$  (its beam magnetic rigidity after the passage through target and stripper foil) and  $y = 0$  (its angular spread is negligible). Figure 4.1-right presents the acceptance plot of one specific nuclide produced in the same nuclear reaction (in the example,  $^{132}\text{Sn}$ ). In both figures three lines are overlaid. The horizontal line at  $y=30$  marks the limit of the angular acceptance of the Super-FRS (average value between  $x$  and  $y$ ). What falls above this line will impinge on the entrance quadrupole. The two vertical lines at  $x=17.35$  and  $x=18.24$  represent the lower and upper acceptance limit for the magnetic rigidity of the Super-FRS tuned in order to transmit the nuclide  $^{132}\text{Sn}$ . What falls inside the narrow rectangle is transmitted; what falls outside will impinge on the iron walls of the first dipole. Specifically, ions with magnetic rigidity above  $18.24 \text{ Tm}$  will be less bent and impinge on the right wall of the dipole<sup>2</sup>; those with  $B\rho < 17.35 \text{ Tm}$  will be more bent and impinge on the left wall of the dipole. Also the beam will impinge on the left wall of the dipole.

Thus, the procedure for the analysis of the data is straightforward. The acceptance plot of the selected fragment is used to determine the  $B\rho$ -window, represented by the narrow rectangle, which gives the limits in magnetic rigidity of the fragments transmitted along the Super-FRS. The window is determined considering that for a give value of the magnetic field the spectrometer has

---

<sup>2</sup> See figure 2.4 for convention on “right” and “left”.

a limitation in magnetic rigidity of  $\pm 2.5\%$ . The position of the window is chosen in order to maximise the counts of the selected fragment inside of it. Once the window is placed, the gating conditions are set, and the events falling inside the four rectangular areas delimited by the three lines can be analysed separately.

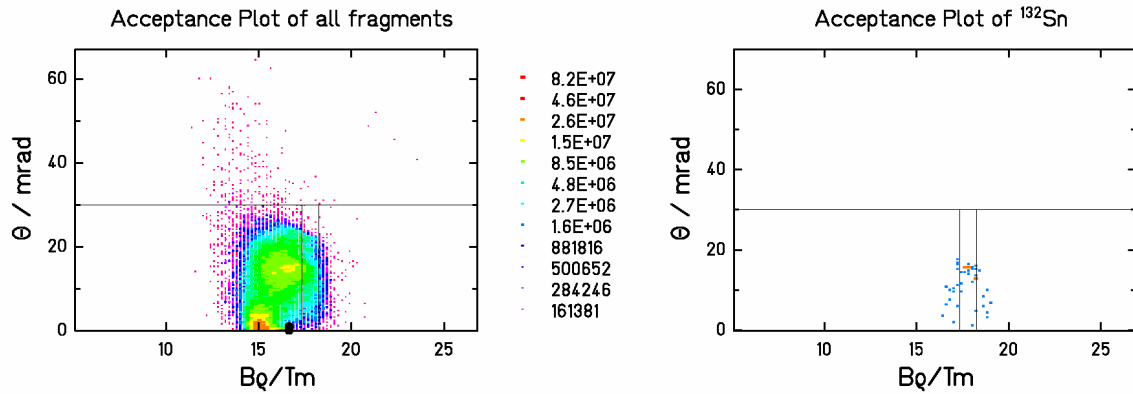


Figure 4.1: Acceptance plot of all fragments (left) and of a specific one (right),  $^{132}\text{Sn}$ . In the example, the reaction  $1.5 \text{ A GeV } ^{238}\text{U}$  beam on tantalum is presented. The beam is represented by the spot at  $x = 16.64$ . The horizontal line at  $y=30$  marks the limit of the angular acceptance of the Super-FRS. Events falling inside the narrow rectangle represent ions that are transmitted along the Super-FRS; what falls outside impinges on the iron walls of the first dipole.

## 4.2 Results

After impinging in the target and in the stripping foil, the intensity of the beam is reduced. Nevertheless the intensity of the surviving beam that enters the 1<sup>st</sup> dipole is still high and concentrated in a specific spot. This requires a devoted shielding. In order to scan the distributions of intensities of surviving beams and fragments, we analysed three extreme cases:

- 1) Selection of a fragment with  $B\rho$  close to the  $B\rho$  of the beam. In this case the surviving beam has to be stopped in some slits.
- 2) Selection of a neutron-rich fragment. In this case the surviving beam will stop in the iron of the 1<sup>st</sup> dipole, on the right wall
- 3) Selection of a proton-rich fragment. In this case the surviving beam will stop in the iron of the 1<sup>st</sup> dipole, on the left wall

As pointed out in section 2.2, for the production of exotic beams the target will be loaded with extremely high power. This reduces the possibilities on the choice of the target to two materials: tantalum and carbon. The study of the target thickness was performed at the Super-FRS group at GSI [Wei04]. The thickness of the target was chosen using the program LISE [Baz02], which calculates the transmission through the Super-FRS of the selected nuclide for different target widths and chose the thickness corresponding to the maximum intensity at the exit.

*Selection of a fragment with  $B\rho$  close to the  $B\rho$  of the beam*

We choose the case of a  $^{238}\text{U}$  beam on a tantalum target, at 1.5 GeV/nucleon, with a primary-beam intensity of  $1 \cdot 10^{12}$  ions/s. The target is  $5.225 \text{ g/cm}^2$  thick, corresponding to 20% of the range of the projectile. The fragment selected is  $^{130}\text{Sn}$ .

ABRABLA gives us the values of the cross sections for nuclear reactions and for electromagnetic interactions:  $\sigma_{nr} = 7.5908 \text{ b}$ ,  $\sigma_{em} = 5.2710 \text{ b}$ . The percentage of electromagnetic interactions and of nuclear reactions occurring in the target and the total number of beam particle consumed can be calculated<sup>3</sup> and are:  $p_{em} = 8.2 \%$ ,  $p_{nr} = 11.8\%$ ,  $p_{reac} = 20.0\%$ . That is to say:  $2.0 \cdot 10^{11}$  beam-particles/s are consumed and  $8.0 \cdot 10^{11}$  beam-particles/s survive. Among these  $2.0 \cdot 10^{11}$  interactions/s 20.6 % of interactions lead to total disintegration of the nucleus, and 79.4 % of interactions lead to the formation of residues (60.0 % of fragmentation reactions and 19.4 % of fission reactions). Fragmentation reactions contribute with one fragment, fission reactions with two. Thus the intensity of the fragments produced in the reactions is  $2.79 \cdot 10^{11}$  ions/s. The distribution of the produced fragments, presented in the chart of the nuclides, is reported in figure

---

<sup>3</sup> The attenuation of the beam in the matter of thickness  $x$  is given by the formula:

$$I_{consumed} = I_{initial} - I_{surviving} = I_{initial} \left( 1 - e^{-k\sigma_{nr}x} \cdot e^{-k\sigma_{em}x} \right) \quad (4.6)$$

where  $k$  contains the Avogadro's number  $N_A$ , the target mass  $M_T$  and density  $\rho_T$ :

$$k = \frac{N_A \cdot \rho_T}{M_T} \quad (4.7)$$

The percentage of nuclear reactions and electromagnetic interactions are given by:

$$p_{nr} = p_{reac} \cdot \frac{\sigma_{nr}}{\sigma_{nr} + \sigma_{em}} \quad \text{and} \quad p_{em} = p_{reac} \cdot \frac{\sigma_{em}}{\sigma_{nr} + \sigma_{em}} \quad (4.8)$$

4.2. The distribution is normalised to the intensity ( $2.79 \cdot 10^{11}$ ). The most produced fragments are  $^{236}\text{U}$  and  $^{237}\text{U}$ . They have a velocity approximately equal to that of the beam and not much spread. This means that they also will produce a well-localised spot of intensity in some point of the dipole wall.

In figure 4.3-left the acceptance plot of all fragments is presented. The plot is normalised to  $2.79 \cdot 10^{11}$ , which corresponds to the intensity of the produced fragments. The sum of the events falling above the horizontal line at  $y=30$  gives the intensity of the fragments stopped in the quadrupole:  $7 \cdot 10^6$  ions/s. The intensity of the fragments entering into the 1<sup>st</sup> dipole of the spectrometer is:  $(2.79 \cdot 10^{11} - 7 \cdot 10^6)$  ions/s  $\cong 2.79 \cdot 10^{11}$  ions/s.

In figure 4.3-right the acceptance plot of the selected fragments is presented. The plot is normalised to  $2.46 \cdot 10^8$ , which corresponds to the intensity of  $^{130}\text{Sn}$ . The gate plotted in the figure represents the best choice for the tuning of the spectrometer in order to transmit the maximum possible intensity of  $^{130}\text{Sn}$ . The width of the window is determined by the constraint in magnetic rigidity, limited to  $\pm 2.5\%$  in the future Super-FRS. Once the gate is established in figure 4.3-right, the same window is imposed in the full acceptance plot of figure 4.3-left. The three windows below the limit of  $y=30$  mrad give the intensity of the fragments falling on the left iron wall of the 1<sup>st</sup> dipole, the intensity of the fragments transmitted, and the intensity of the fragments falling on the right iron wall of the 1<sup>st</sup> dipole, respectively. Numerically we have: fragments going in the left iron wall of the dipole (surviving beam excluded):  $2.04 \cdot 10^{11}$  ions/s; fragments going in the right iron wall of the dipole:  $2.4 \cdot 10^{10}$  ions/s; fragments transmitted:  $5.1 \cdot 10^{10}$  ions/s. The black spot in figure 4.3-right at  $x=16.64$  represents the surviving beam. In order to avoid the transmission of the surviving beam, slits have to be placed after the first dipole. The slit on the left side is represented in figure 4.3-left by the vertical black thick line. So, the slit gets the intensity of  $8.0 \cdot 10^{11}$  ions/s in one localised spot, plus a minor contribution of fragments with the same magnetic rigidity of the beam.

Figure 4.4 depicts the distribution of the fragments stopping in the dipole walls, represented in the chart of the nuclides. In figure 4.5 the nuclides impinging on the dipole walls are presented integrated over the atomic number, versus their velocity. These plots are important to have an idea of the possible radiation damage of the superconducting magnets. Finally, in figure 4.6, we present a contour plot of the radii of the trajectories of the fragments, entering the 1<sup>st</sup> dipole of the Super-FRS, tuned to transmit the selected fragment ( $^{130}\text{Sn}$ ). The central trajectory has a radius of 12.5 meters.

All the numerical results are collected in table 4.1. Table 4.2 collects also all other possibilities of different tuning of the magnets. The magnetic rigidity is scaled in steps of 5%.

In section 3.5, we commented that the yields of fragments below  $Z \cong 10$  is underestimated. Light fragments are produced in multifragmentation events with high multiplicity, which is not taken into account in ABRABLA. These very light fragments are characterized by a large spectrum of velocities. The experience with experiments performed with full-acceptance spectrometers (see for instance ref. [Sch96]) in the 1GeV region shows that their velocity can vary between 0 and 4 cm/ns in the centre of mass. Since the velocity originates mostly in the abrasion process, we can safely assume that the range of velocities remains practically the same also for 1.5 GeV beam energy. Applying this to our case, we would obtain that their magnetic rigidity can vary between 12 Tm to 19 Tm. As a consequence, the higher intensity of these fragments has to be distributed among a large spectrum of magnetic rigidities, i.e. of trajectories. This makes the flux rather low. Therefore, as a first estimation of the yields – that is the purpose of this work – light fragments are neglected. Also, the flux of neutrons arising in central collisions, leading to the full disintegration of the nuclei, is neglected. Devoted studies, experimental and theoretical, are being performed separately [Feh02].

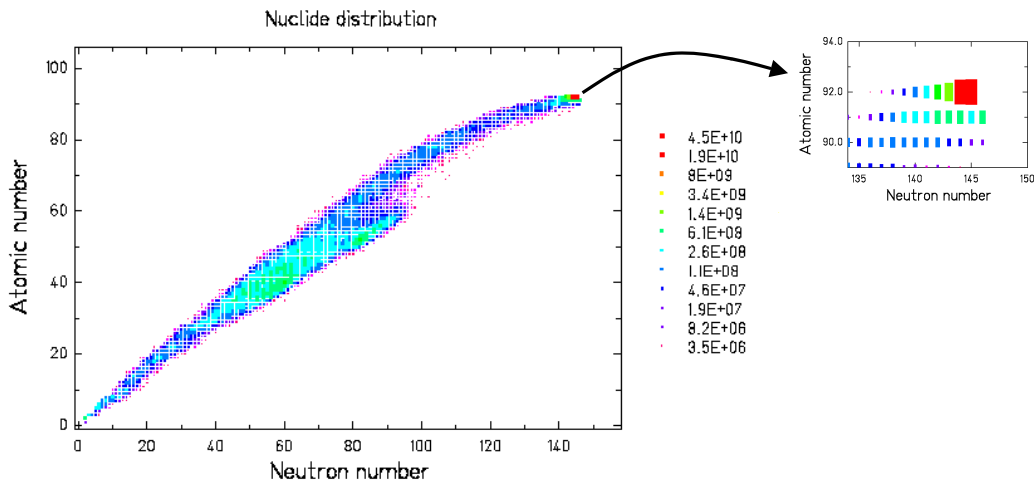


Figure 4.2: Distribution of produced fragments in the reaction  $^{238}\text{U}$  on tantalum, presented in the chart of the nuclides. The beam has an initial energy of 1.5 GeV per nucleon, and intensity  $1 \cdot 10^{12}$  particle per second. The coloured scale gives the intensity in ions/second.

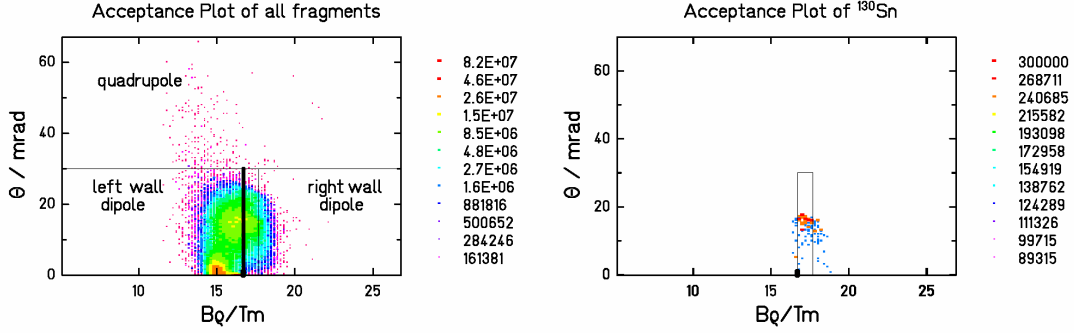


Figure 4.3: Acceptance plot of all fragments (left) and of the selected one (right),  $^{130}\text{Sn}$ , for the reaction  $1.5 \text{ A GeV } ^{238}\text{U}$  beam on tantalum. The horizontal line at  $y=30$  marks the limit of the angular acceptance of the Super-FRS. Events falling inside the narrow rectangle represent ions that are transmitted along the Super-FRS; what falls outside impinge on the iron walls of the first dipole. The beam is represented by the spot at  $x = 16.64$ . What falls on the black vertical line at  $x = 16.64$  is stopped in the slits. The coloured scales give the intensity in ions/second.

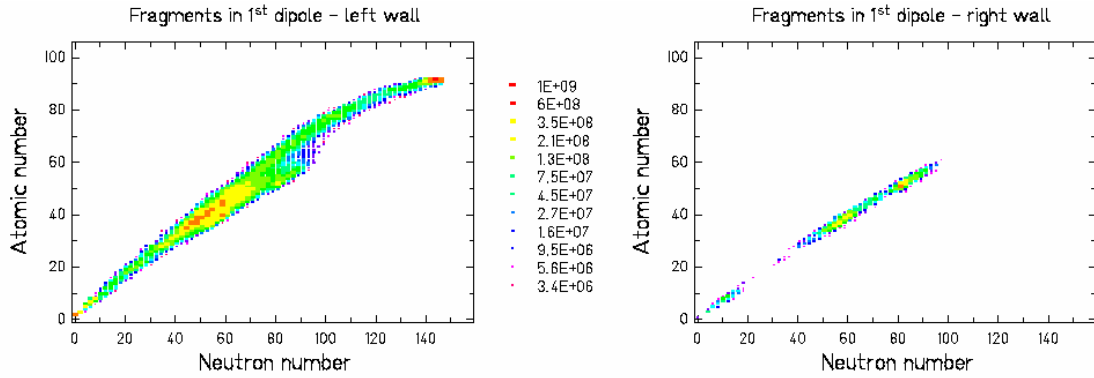


Figure 4.4: Distributions of fragments stopped in the iron walls of the 1<sup>st</sup> dipole. The coloured scale gives the intensity in ions/second.

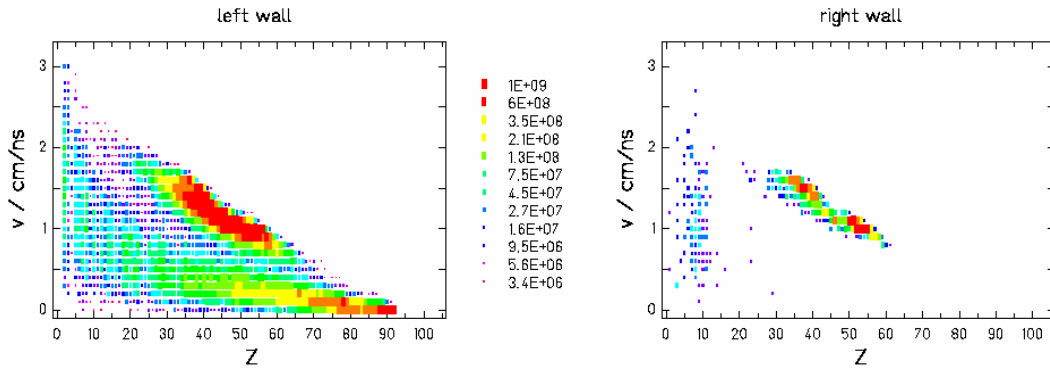


Figure 4.5: Distributions of velocities of the fragments stopped in the iron walls of the 1<sup>st</sup> dipole. The coloured scale gives the intensity in ions/second.

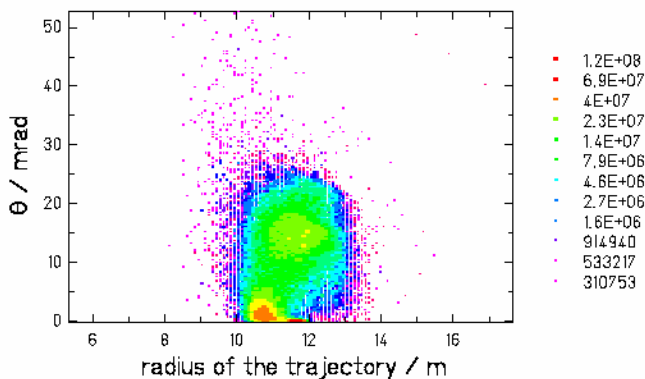


Figure 4.6: Distribution of the radii of the trajectories of fragments produced in the reactions, when the magnetic field is tuned to transmit  $^{130}\text{Sn}$ . The coloured scale gives the intensity in ions/second.

#### *Selection of a neutron-rich fragment*

We choose the case of a  $^{48}\text{Ca}$  beam on carbon target, at 1.5 GeV/nucleon, with a primary-beam intensity of  $1 \cdot 10^{12}$  ions/s. The target is  $6 \text{ g/cm}^2$  thick, corresponding to about 14% of the range. The selected fragment is  $^{11}\text{Li}$ .

The results given by the simulation performed with ABRABLA were analysed as described for the previous case. In figure 4.7 the production of nuclides is presented on the chart of the nuclides. Please note that in this case great part of the products is constituted of light masses. In this case the use of the abrasion-evaporation code is in principle inappropriate. In fact, many collisions introduce enough energy to induce the multifragmentation of the nucleus. In order to improve the prediction of the ABRABLA code for this case, we introduced an intermediate reaction step in-between abrasion and evaporation that depicts the “break-up” of the nucleus into several fragments. This intermediate stage, was introduced as a simple parameterisation deduced from experimental data. The study and parameterisation of the break-up stage was performed in a previous work [Sch02]. The parameterisation of ref. [Sch02] takes into account the consumption of energy burned up in the multifragmentation of the nucleus, but does not follow explicitly the history of all the fragments formed at once in the process. In every event, the successive deexcitation of only one fragment formed in the break-up is performed. Although the introduction of the break-up stage improves considerably the prediction (see ref. [Sch02]), results for fragments with  $Z \leq 4$  are underestimated, since the production of protons, alphas and light nuclides is dominated by the evaporation and by multifragmentation events with high multiplicity. Devoted studies that consider the products of the evaporation and of the total

disassembly of the nucleus have to be performed. On the other hand, we must consider that the most dangerous residual nuclei, both in terms of radioactivity and of radiation damage, are the heavier fragments. So the results presented here are indeed of great interest for the safety issue.

The selected fragment ( $^{11}\text{Li}$ ) has such a low formation cross-section that the simulation of its production with sufficiently high statistic would require a long computing time. In order to bypass this difficulty we have reproduced the magnetic rigidity of  $^{11}\text{Li}$  exploiting the velocity distribution of  $^9\text{Li}$ . This is justified by the fact that all the lithium isotopes are produced with the same reaction mechanisms (fragmentation). As explained in section 3.2, the formation of fragments with similar mass is expected to lead to similar velocities. The scattered plot of the magnetic rigidity of  $^{11}\text{Li}$  is used only to set the gate that defines the transmitted fragments (see figure 4.8). The magnetic rigidity of  $^{11}\text{Li}$  is so high (due to the high value of  $A/Z$ ) that the bulk of the production has a lower  $B\rho$  and falls consequently on the left wall of the 1<sup>st</sup> dipole. Therefore, the distribution of fragments impinging on the right iron wall of the first dipole is equivalent to the whole production presented in figure 4.7. The velocity distribution of fragments impinging on the right iron wall of the first dipole is presented in figure 4.9. In figure 4.10 the distribution of the radii of the trajectories of the produced fragments is depicted.

The numerical results are collected in Table 4.3. Table 4.4 collects all other possibilities of different tuning of the magnets. The magnetic rigidity is scaled in steps of 5%.

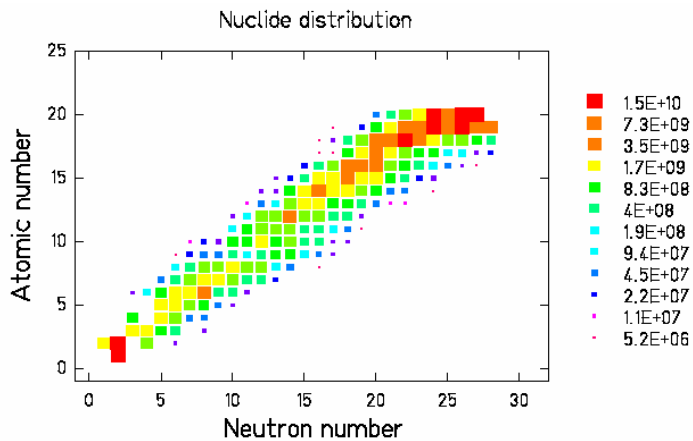


Figure 4.7: Distribution of produced fragments in the reaction  $^{48}\text{Ca}$  on carbon, presented on the chart of the nuclides. The beam has an initial energy of 1.5 GeV per nucleon, and intensity  $1 \cdot 10^{12}$  particles per second. The coloured scale gives the intensity in ions/second.

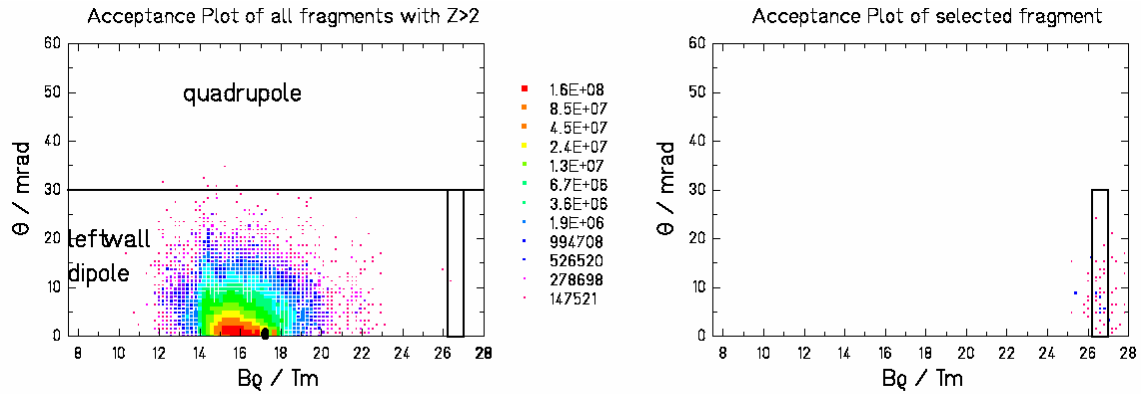


Figure 4.8: Left: Acceptance plot of all fragments for the reaction  $1.5 \text{ A GeV } ^{48}\text{Ca}$  beam on carbon. The coloured scale gives the intensity in ions/second. The horizontal line at  $y=30$  marks the limit of the angular acceptance of the Super-FRS. The few events falling inside the narrow rectangle represent ions that are transmitted along the Super-FRS; what falls outside impinges on the iron walls of the first dipole. The beam is represented by the spot at  $x = 17.20$ . Right: Acceptance of the selected fragment,  $^{11}\text{Li}$ . The plot was constructed using the angular and velocity distributions of  $^9\text{Li}$ . The coloured scale gives the intensity in arbitrary units.

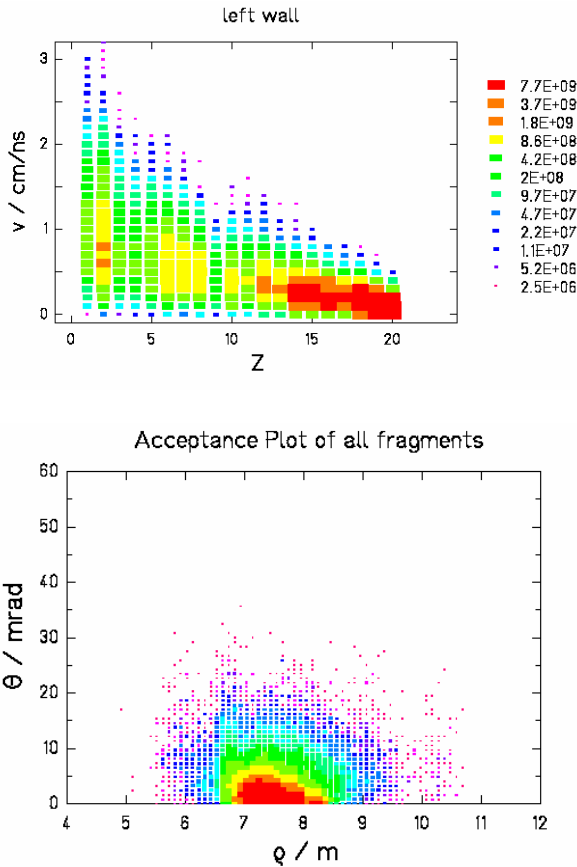


Figure 4.9: Distributions of velocities of the fragments stopped in the left iron wall of the 1<sup>st</sup> dipole. The coloured scale gives the intensity in ions/second.

Figure 4.10: Distribution of the radii of the trajectories of fragments produced in the reactions, when the magnetic field is tuned to transmit  $^{11}\text{Li}$ .

### Selection of a proton-rich fragment

We choose the case of a  $^{238}\text{U}$  beam on carbon target, at 1.5 GeV/nucleon, with a primary beam intensity of  $1 \cdot 10^{12}$  ions/s. The target is  $4 \text{ g/cm}^2$  thick, corresponding to about 10% of the range. The selected fragment is  $^{100}\text{Sn}$ .

The production of nuclides given by the simulation performed with ABRABLA is presented in the chart of the nuclides in figure 4.11. The data were analysed as described previously. Please note that the nuclides with highest production are  $^{237}\text{U}$  and  $^{236}\text{U}$ . They have a rather narrow velocity distribution and consequently their magnetic rigidity will be concentrated in a short range of values.

As in the previous case, here the selected fragment ( $^{100}\text{Sn}$ ) has such a low formation cross-section that the simulation of its production with sufficiently high statistic would require a too long computing time. Therefore, we have reproduced the magnetic rigidity of  $^{100}\text{Sn}$  exploiting the velocity distribution of a close tin isotope. In fact, close isotopes are produced with the same reaction mechanisms – again fragmentation – and have therefore similar velocities. This assumption was verified by checking the spectra of the isotopes close to  $^{100}\text{Sn}$ . Neutron-rich isotopes were excluded because they are produced in fission reactions. The scatter plot of the magnetic rigidity of  $^{100}\text{Sn}$  is used only to set the gate that defines the transmitted fragments (see figure 4.12). In contrast to the case of the neutron-rich  $^{11}\text{Li}$ , whose magnetic rigidity is very high, the magnetic rigidity of the proton-rich  $^{100}\text{Sn}$  is not particularly low; for example, it is similar to that of many light fragments, which have the same  $A/Z$  ratio.

We present the distribution of fragments impinging on the right and left iron walls of the first dipole in figure 4.13, and their velocity, in figure 4.14. In figure 4.15 the distribution of the radii of the trajectories of the produced fragments is depicted.

The numerical results are collected in Table 4.5. Table 4.6 collects all other possibilities of different tuning of the magnets. The magnetic rigidity is scaled in steps of 5%.

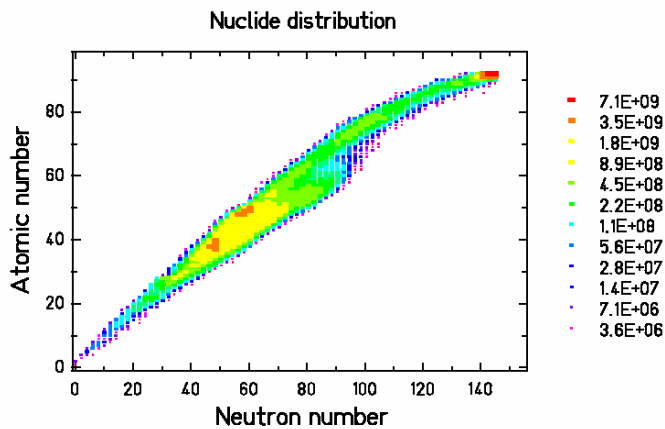


Figure 4.11: Distribution of produced fragments in the reaction  $^{238}\text{U}$  on carbon, presented on the chart of the nuclides. The beam has an initial energy of 1.5 GeV per nucleon, and intensity  $1 \cdot 10^{12}$  particles per second.

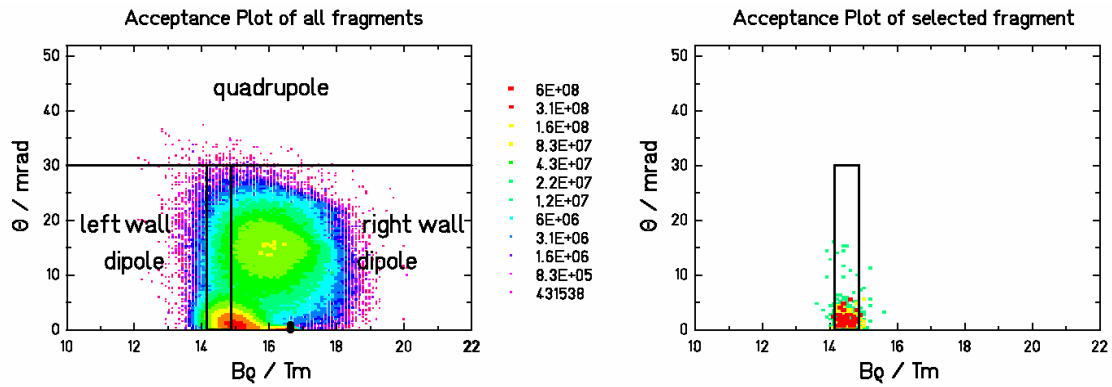


Figure 4.12: Left: Acceptance plot of all fragments for the reaction  $1.5 A \text{ GeV } ^{238}\text{U}$  beam on carbon. The coloured scale gives the intensity in ions/second. The horizontal line at  $y=30$  marks the limit of the angular acceptance of the Super-FRS. Events falling inside the narrow rectangle represent ions that are transmitted along the Super-FRS; what falls outside impinge on the iron walls of the first dipole. The beam is represented by the spot at  $x = 16.64$ . Right: Acceptance of the selected fragment,  $^{100}\text{Sn}$ . The plot was constructed using the angular and velocity distributions of close tin isotopes. The coloured scale gives the intensity in arbitrary units.

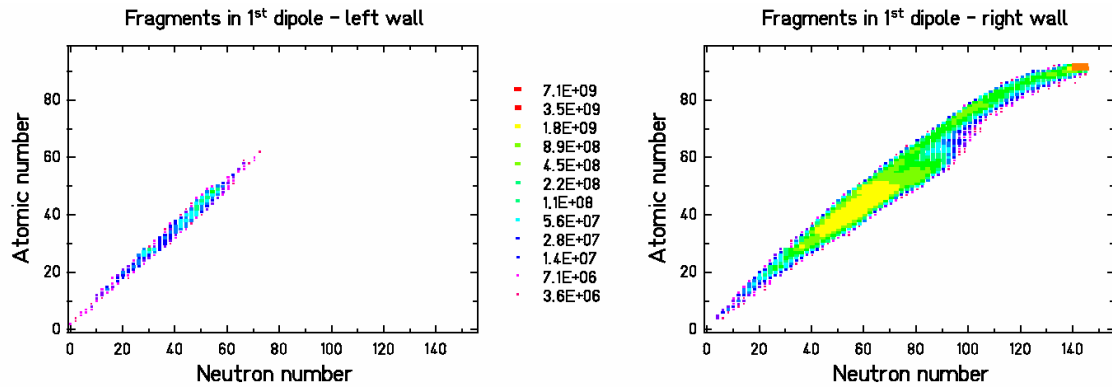


Figure 4.13: Distributions of fragments stopped in the iron walls of the 1st dipole.

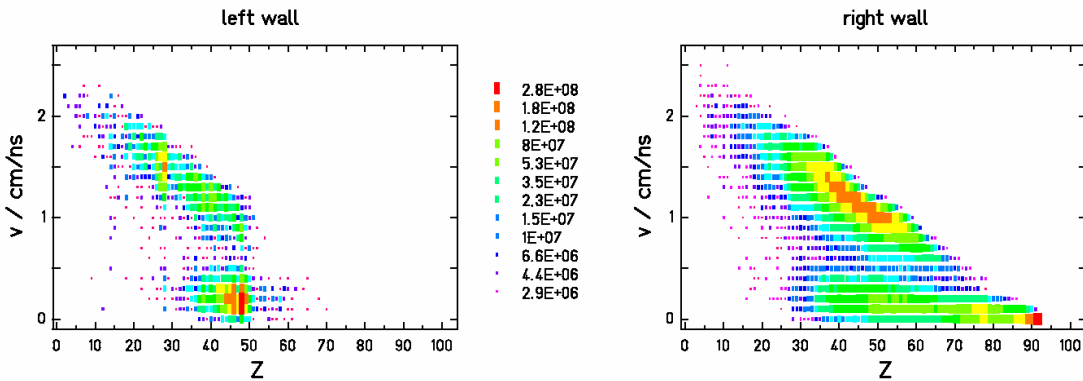


Figure 4.14: Distributions of velocities of the fragments stopped in the iron walls of the 1st dipole.

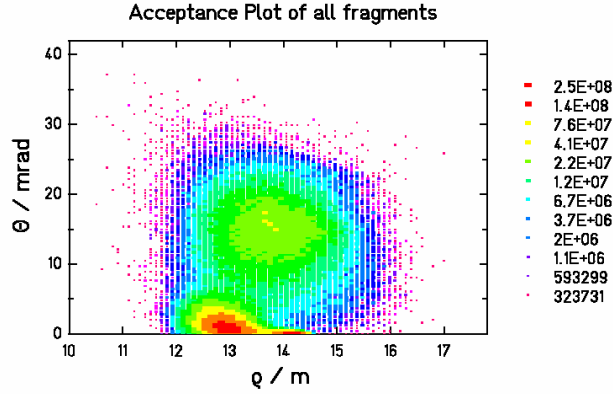


Figure 4.15: Distribution of the radii of the trajectories of fragments produced in the reactions, when the magnetic field is tuned to transmit  $^{100}\text{Sn}$ .

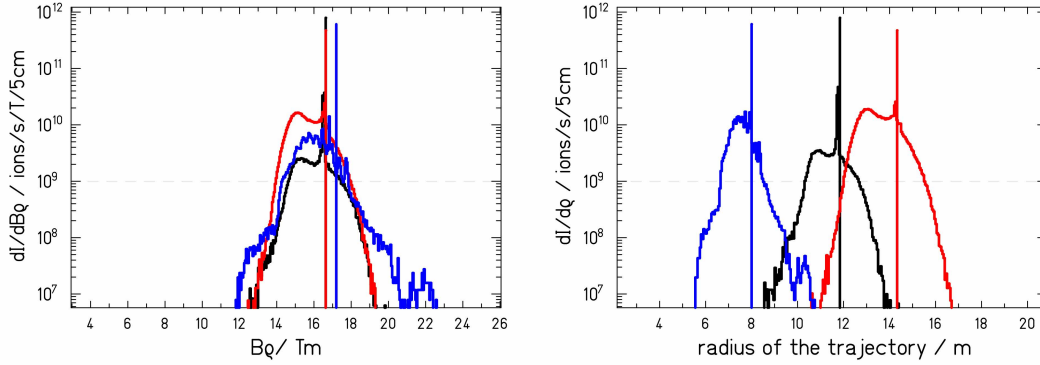
### 4.3 Discussion

The starting results of this work are the map of the residual nuclides produced at the Super-FRS and their velocities. The distributions of residual ions and velocities were presented in figures 4.2, 4.5, 4.7, 4.9, 4.11, and 4.14 for three key cases. These results are essential for the design and handling of the Super-FRS, to control the radiation damage and to avoid the quenching of the magnets. Successively, the results have been worked out to release information on the distribution of magnetic rigidities and trajectories of the ions. This information is useful for the design of the shielding around the Super-FRS. In this section we want to comment on the latter results.

In figure 4.16-left we present the distribution of the magnetic rigidities for the three cases analysed. The three vertical lines give the intensity of the surviving primary beams. The horizontal dashed line represents the intensity available at the actual GSI facility for a  $^{238}\text{U}$  primary beam. Please note that the staggering of the curves is not due to statistical fluctuations. Specifically the peaks close to the magnetic rigidities of the beams are due to the most produced isotopes ( $^{236,237}\text{U}$ ,  $^{44-47}\text{Ca}$ ,  $^{41-47}\text{K}$ ). On the right side of the figure the corresponding distributions of the radii of the trajectories, when the magnetic field is tuned in order to transmit the selected fragments, are presented. The magnetic rigidities of the selected fragments are around 16.8 Tm (for  $^{238}\text{U}$  on Ta), 26.6 Tm (for  $^{48}\text{Ca}$  on C) and 14.5 Tm (for  $^{238}\text{U}$  on C). In tables 4.2, 4.4, 4.6 we collected the results for all the other possible tuning of the magnet. In correspondence to these tunings the distributions of the radii shift, as shown in figure 4.17. Figure 4.18 collects all the distributions for the three key cases.

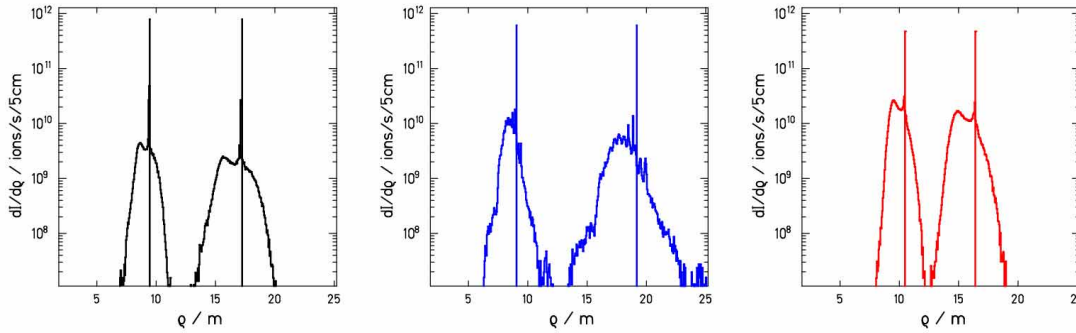
Combining the results we come to the conclusions that intensities above  $10^{10}$  are expectable in the region delimited by trajectories with radii between 7.2 m and 19.3 m. In particular, between 8 m and 19.3

m intensities around  $7 \cdot 10^{11}$  have to be expected. Therefore the region around the 1<sup>st</sup> dipole of the Super-FRS will be highly radioactive and adequate shielding have to be considered for the zone delimited by the circles of radii 7.2 m and 19.3 m.



Figure

4.16: Left: Distributions of the magnetic rigidities for the cases presented in the previous section: 1.5 A GeV  $^{48}\text{Ca}$  on C (blue), 1.5 A GeV  $^{238}\text{U}$  on C (red), 1.5 A GeV  $^{238}\text{U}$  on Ta (black). Right: Corresponding distributions of the radii of the trajectories, when the magnetic field is tuned in order to transmit the selected fragments ( $^{11}\text{Li}$ ,  $^{100}\text{Sn}$ ,  $^{130}\text{Sn}$ , respectively). The 5-cm step in the unit of the y axis is due to the width of the channel of the x axis of figures 4.3, 4.8, 4.12, 4.6, 4.10, 4.15.



Figure

4.17: Left: Distributions of the radii of the trajectories for the residues of 1.5 A GeV  $^{238}\text{U}$  on Ta, when the magnet is tuned to 12.03 Tm (curve on the right) and to 21.92 Tm (curve on the left). See table 4.2. Centre: Distributions of the radii of the trajectories for the residues of 1.5 A GeV  $^{48}\text{Ca}$  on C, when the magnet is tuned to 11.13 Tm (curve on the right) and to 23.57 Tm (curve on the left). See table 4.4. Right: Distributions of the radii of the trajectories for the residues of 1.5 A GeV  $^{238}\text{U}$  on C, when the magnet is tuned to 12.65 Tm (curve on the right) and to 19.84 Tm (curve on the left). See table 4.6. The 5-cm step in the unit of the y axis is due to the width of the channel of the x axis of the  $\theta$ - $B\rho$  scatter-plot spectra.

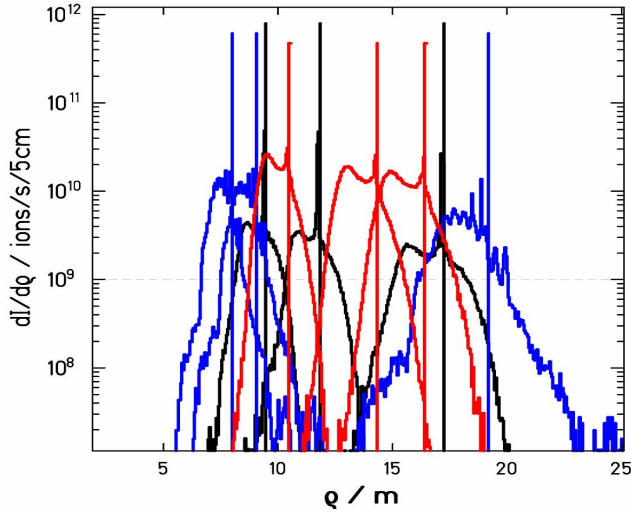


Figure 4.18: All the distributions of the radii of the trajectories for the residues of 1.5 A GeV  $^{238}\text{U}$  on Ta, of 1.5 A GeV  $^{48}\text{Ca}$  on C, and of 1.5 A GeV  $^{238}\text{U}$  on C. The 5-cm step in the unit of the y axis is due to the width of the channel of the x axis of the  $\theta$ - $B\rho$  scatter-plot spectra.

#### *Presentation of the numerical results*

All the numerical results are gathered in the following tables. They are based on the cross sections evaluated with a computational tool. The reliability of the code used in this work is rather good for the evaluation of cross sections of nuclides close to the projectile (in the order of 20% relative error for a specific isotope) but it gets worse as the mass of the residue decreases. For nuclides far from the projectile it can be off by a factor of two for some specific nuclide. Therefore it is rather difficult to specify the error of the calculations. However, one must consider that the purpose of this work is to know the order of magnitude of the produced radioactive particles, especially the heaviest ones, which are the most dangerous in terms of safety aspects. Moreover, the general overview of the production is rather realistic.

Concerning the presentation of the numbers in the tables, they were automatically generated. So, please do not assume that the error is on the last digit.

TABLE 4.1

Summary of numerical results for the case of a  $^{238}\text{U}$  beam on a tantalum target, at 1.5 GeV/nucleon, with a primary-beam intensity of  $1 \cdot 10^{12}$  ions/s. The target is  $5.225 \text{ g/cm}^2$  thick, corresponding to 20% of the range of the projectile. The selected fragment is  $^{130}\text{Sn}$ .

GENERAL:

Percentage of beam performing nuclear reactions = 11.8 %

Percentage of beam performing electromagnetic interactions = 8.2 %

Total percentage of beam performing reactions = 20.0 %

Percentage of interactions that lead to total disintegration of the nucleus = 20.6 %

Percentage of interactions that lead to the formation of residues = 79.4 %

Among which: 60.0 % fragmentation, 19.4 % fission

Initial beam intensity =  $1 \cdot 10^{12}$  ions/s

Intensity of surviving beam =  $8.0 \cdot 10^{11}$  ions/s

Intensity of fragments produced in the reactions =  $2.79 \cdot 10^{11}$  ions/s

Intensity of fragments stopped in the quadrupole =  $7 \cdot 10^6$  ions/s

SELECTED CASE:

Intensity of fragments going in the left iron wall of the dipole (diffuse) =  $2.04 \cdot 10^{11}$  ions/s

Intensity of fragments going in the right iron wall of the dipole (diffuse) =  $2.4 \cdot 10^{10}$  ions/s

Intensity of fragments transmitted =  $5.1 \cdot 10^{10}$  ions/s

Intensity of surviving beam stopped in the slits (one spot) =  $8.0 \cdot 10^{11}$  ions/s

TABLE 4.2

Predicted intensities for the case of a  $^{238}\text{U}$  beam on tantalum target, at 1.5 GeV/nucleon, with a primary beam intensity of  $1 \cdot 10^{12}$  ions/s. The target is  $5.225 \text{ g/cm}^2$  thick, corresponding to 20% of the range. The bin in magnetic rigidity is  $\pm 2.5\%$  around the values in the 1<sup>st</sup> column, corresponding to the momentum acceptance of the Super-FRS. The corresponding transmitted fragments are in the second column. The other columns give the intensities of the fragments stopped in the dipole walls and of the surviving beam.

Selected Bp (Tm)	Intensity of transmitted fragments (ions/s)	Intensity of fragments stopped in the dipole (ions/s)	Intensity of fragments stopped in the dipole left wall (ions/s)	Intensity of fragments stopped in the dipole right wall (ions/s)	Intensity of the surviving beam (ions/s)	Place where the surviving beam is stopped
11.4427	0	$2.80 \cdot 10^{11}$	0	$2.80 \cdot 10^{11}$	$8.00 \cdot 10^{11}$	DIPOLE LEFT
12.0295	$4.55 \cdot 10^7$	$2.80 \cdot 10^{11}$	$4.55 \cdot 10^6$	$2.80 \cdot 10^{11}$	$8.00 \cdot 10^{11}$	DIPOLE LEFT
12.6464	$2.09 \cdot 10^8$	$2.79 \cdot 10^{11}$	$5.00 \cdot 10^7$	$2.79 \cdot 10^{11}$	$8.00 \cdot 10^{11}$	DIPOLE LEFT
13.2949	$7.51 \cdot 10^8$	$2.79 \cdot 10^{11}$	$2.59 \cdot 10^8$	$2.79 \cdot 10^{11}$	$8.00 \cdot 10^{11}$	DIPOLE LEFT
13.9767	$4.66 \cdot 10^9$	$2.75 \cdot 10^{11}$	$1.01 \cdot 10^9$	$2.74 \cdot 10^{11}$	$8.00 \cdot 10^{11}$	DIPOLE LEFT
14.6935	$4.47 \cdot 10^{10}$	$2.35 \cdot 10^{11}$	$5.67 \cdot 10^9$	$2.29 \cdot 10^{11}$	$8.00 \cdot 10^{11}$	DIPOLE LEFT
15.4470	$7.65 \cdot 10^{10}$	$2.03 \cdot 10^{11}$	$5.04 \cdot 10^{10}$	$1.53 \cdot 10^{11}$	$8.00 \cdot 10^{11}$	DIPOLE LEFT
16.2391	$7.65 \cdot 10^{10}$	$2.03 \cdot 10^{11}$	$1.27 \cdot 10^{11}$	$7.66 \cdot 10^{10}$	$8.00 \cdot 10^{11}$	SLIT LEFT
17.0719	$5.21 \cdot 10^{10}$	$2.27 \cdot 10^{11}$	$2.03 \cdot 10^{11}$	$2.44 \cdot 10^{10}$	$8.00 \cdot 10^{11}$	SLIT RIGHT
17.9474	$2.09 \cdot 10^{10}$	$2.58 \cdot 10^{11}$	$2.55 \cdot 10^{11}$	$3.08 \cdot 10^9$	$8.00 \cdot 10^{11}$	DIPOLE RIGHT
18.8678	$2.60 \cdot 10^9$	$2.77 \cdot 10^{11}$	$2.77 \cdot 10^{11}$	$4.81 \cdot 10^8$	$8.00 \cdot 10^{11}$	DIPOLE RIGHT
19.8354	$8.65 \cdot 10^7$	$2.80 \cdot 10^{11}$	$2.79 \cdot 10^{11}$	$3.94 \cdot 10^8$	$8.00 \cdot 10^{11}$	DIPOLE RIGHT
20.8526	$1.82 \cdot 10^7$	$2.80 \cdot 10^{11}$	$2.79 \cdot 10^{11}$	$3.76 \cdot 10^8$	$8.00 \cdot 10^{11}$	DIPOLE RIGHT
21.9220	$1.36 \cdot 10^7$	$2.80 \cdot 10^{11}$	$2.79 \cdot 10^{11}$	$3.63 \cdot 10^8$	$8.00 \cdot 10^{11}$	DIPOLE RIGHT
23.0462	0	$2.80 \cdot 10^{11}$	$2.80 \cdot 10^{11}$	0	$8.00 \cdot 10^{11}$	DIPOLE RIGHT

TABLE 4.3

Summary of numerical results for the case of a  $^{48}\text{Ca}$  beam on a carbon target, at 1.5 GeV/nucleon, with a primary-beam intensity of  $1 \cdot 10^{12}$  ions/s. The target is  $6.0 \text{ g/cm}^2$  thick, corresponding to about 14% of the range of the projectile. The selected fragment is  $^{11}\text{Li}$ .

GENERAL:

Percentage of beam performing nuclear reactions = 38.90 %

Percentage of beam performing electromagnetic interactions = 0.12 %

Total percentage of beam performing reactions = 39.02 %

Percentage of interactions that lead to total disintegration of the nucleus = 26.4 %

Percentage of interactions that lead to the formation of residues = 73.6 %

Among which: 100.0 % fragmentation, 0 % fission

Initial beam intensity =  $1 \cdot 10^{12}$  ions/s

Intensity of surviving beam =  $6.10 \cdot 10^{11}$  ions/s

Intensity of fragments produced in the reactions =  $2.87 \cdot 10^{11}$  ions/s

Intensity of fragments stopped in the quadrupole =  $4.1 \cdot 10^8$  ions/s

SELECTED CASE:

Intensity of fragments going in the left iron wall of the dipole (diffuse) =  $2.866 \cdot 10^{11}$  ions/s

Intensity of fragments going in the right iron wall of the dipole (diffuse) =  $3 \cdot 10^6$  ions/s

Intensity of fragments transmitted =  $7 \cdot 10^6$  ions/s

Intensity of surviving beam stopped the left wall of the dipole (one spot) =  $6.10 \cdot 10^{11}$  ions/s

TABLE 4.4

Predicted intensities for the case of a  $^{48}\text{Ca}$  beam on carbon target, at 1.5 GeV/nucleon, with a primary beam intensity of  $1 \cdot 10^{12}$  ions/s. The target is  $6.0 \text{ g/cm}^2$  thick, corresponding to 14% of the range. The bin in magnetic rigidity is  $\pm 2.5\%$  around the values in the 1<sup>st</sup> column, corresponding to the momentum acceptance of the Super-FRS. The corresponding transmitted fragments are in the second column. The other columns give the intensities of the fragments stopped in the dipole walls and of the surviving beam.

Selected Bp (Tm)	Intensity of transmitted fragments (ions/s)	Intensity of fragments stopped in the dipole (ions/s)	Intensity of fragments stopped in the dipole left wall (ions/s)	Intensity of fragments stopped in the dipole right wall (ions/s)	Intensity of the surviving beam (ions/s)	Place where the surviving beam is stopped
10.59095	0	$2.87 \cdot 10^{11}$	0	$2.87 \cdot 10^{11}$	$6.10 \cdot 10^{11}$	DIPOLE LEFT
11.13407	$1.65 \cdot 10^7$	$2.87 \cdot 10^{11}$	0	$2.87 \cdot 10^{11}$	$6.10 \cdot 10^{11}$	DIPOLE LEFT
11.70505	$7.41 \cdot 10^7$	$2.87 \cdot 10^{11}$	$1.65 \cdot 10^7$	$2.87 \cdot 10^{11}$	$6.10 \cdot 10^{11}$	DIPOLE LEFT
12.30531	$7.90 \cdot 10^8$	$2.86 \cdot 10^{11}$	$9.05 \cdot 10^7$	$2.86 \cdot 10^{11}$	$6.10 \cdot 10^{11}$	DIPOLE LEFT
12.93635	$5.42 \cdot 10^9$	$2.82 \cdot 10^{11}$	$8.81 \cdot 10^8$	$2.81 \cdot 10^{11}$	$6.10 \cdot 10^{11}$	DIPOLE LEFT
13.59975	$2.10 \cdot 10^{10}$	$2.66 \cdot 10^{11}$	$6.30 \cdot 10^9$	$2.60 \cdot 10^{11}$	$6.10 \cdot 10^{11}$	DIPOLE LEFT
14.29717	$5.60 \cdot 10^{10}$	$2.31 \cdot 10^{11}$	$2.73 \cdot 10^{10}$	$2.04 \cdot 10^{11}$	$6.10 \cdot 10^{11}$	DIPOLE LEFT
15.03036	$7.62 \cdot 10^{10}$	$2.11 \cdot 10^{11}$	$8.33 \cdot 10^{10}$	$1.28 \cdot 10^{11}$	$6.10 \cdot 10^{11}$	DIPOLE LEFT
15.80115	$6.52 \cdot 10^{10}$	$2.22 \cdot 10^{11}$	$1.59 \cdot 10^{11}$	$6.24 \cdot 10^{10}$	$6.10 \cdot 10^{11}$	DIPOLE LEFT
16.61147	$4.16 \cdot 10^{10}$	$2.46 \cdot 10^{11}$	$2.25 \cdot 10^{11}$	$2.09 \cdot 10^{10}$	$6.10 \cdot 10^{11}$	SLIT LEFT
17.46334	$1.41 \cdot 10^{10}$	$2.73 \cdot 10^{11}$	$2.66 \cdot 10^{11}$	$6.78 \cdot 10^9$	$6.10 \cdot 10^{11}$	SLIT RIGHT
18.35889	$3.23 \cdot 10^9$	$2.84 \cdot 10^{11}$	$2.80 \cdot 10^{11}$	$3.55 \cdot 10^9$	$6.10 \cdot 10^{11}$	DIPOLE RIGHT
19.30037	$8.35 \cdot 10^8$	$2.86 \cdot 10^{11}$	$2.84 \cdot 10^{11}$	$2.72 \cdot 10^9$	$6.10 \cdot 10^{11}$	DIPOLE RIGHT
20.29014	$2.47 \cdot 10^8$	$2.87 \cdot 10^{11}$	$2.84 \cdot 10^{11}$	$2.47 \cdot 10^9$	$6.10 \cdot 10^{11}$	DIPOLE RIGHT
21.33066	$9.05 \cdot 10^7$	$2.87 \cdot 10^{11}$	$2.85 \cdot 10^{11}$	$2.38 \cdot 10^9$	$6.10 \cdot 10^{11}$	DIPOLE RIGHT
22.42454	$4.94 \cdot 10^7$	$2.87 \cdot 10^{11}$	$2.85 \cdot 10^{11}$	$2.33 \cdot 10^9$	$6.10 \cdot 10^{11}$	DIPOLE RIGHT
23.57451	$2.06 \cdot 10^7$	$2.87 \cdot 10^{11}$	$2.85 \cdot 10^{11}$	$2.31 \cdot 10^9$	$6.10 \cdot 10^{11}$	DIPOLE RIGHT
24.78346	0	$2.87 \cdot 10^{11}$	$2.85 \cdot 10^{11}$	$2.31 \cdot 10^9$	$6.10 \cdot 10^{11}$	DIPOLE RIGHT

TABLE 4.5

Summary of numerical results for the case of a  $^{238}\text{U}$  beam on a carbon target, at 1.5 GeV/nucleon, with a primary-beam intensity of  $1 \cdot 10^{12}$  ions/s. The target is  $4.0 \text{ g/cm}^2$  thick, corresponding to about 10% of the range of the projectile. The selected fragment is  $^{100}\text{Sn}$ .

GENERAL:

Percentage of beam performing nuclear reactions = 51.90 %

Percentage of beam performing electromagnetic interactions = 0.75 %

Total percentage of beam performing reactions = 52.65 %

Percentage of interactions that lead to total disintegration of the nucleus = 0.01 %

Percentage of interactions that lead to the formation of residues = 99.9 %

Among which: 57.7 % fragmentation, 42.3 % fission

Initial beam intensity =  $1 \cdot 10^{12}$  ions/s

Intensity of surviving beam =  $4.73 \cdot 10^{11}$  ions/s

Intensity of fragments produced in the reactions =  $7.27 \cdot 10^{11}$  ions/s

Intensity of fragments stopped in the quadrupole =  $4.6 \cdot 10^8$  ions/s

SELECTED CASE:

Intensity of fragments going in the left iron wall of the dipole (diffuse) =  $3.05 \cdot 10^{10}$  ions/s

Intensity of fragments going in the right iron wall of the dipole (diffuse) =  $5.71 \cdot 10^{11}$  ions/s

Intensity of fragments transmitted =  $1.25 \cdot 10^{11}$  ions/s

Intensity of surviving beam stopped the right wall of the dipole (one spot) =  $4.73 \cdot 10^{11}$  ions/s

TABLE 4.6

Predicted intensities for the case of a  $^{238}\text{U}$  beam on carbon target, at 1.5 GeV/nucleon, with a primary beam intensity of  $1 \cdot 10^{12}$  ions/s. The target is  $4.0 \text{ g/cm}^2$  thick, corresponding to 10% of the range. The bin in magnetic rigidity is  $\pm 2.5\%$  around the values in the 1<sup>st</sup> column, corresponding to the momentum acceptance of the Super-FRS. The corresponding transmitted fragments are in the second column. The other columns give the intensities of the fragments stopped in the dipole walls and of the surviving beam.

Selected Bp (Tm)	Intensity of transmitted fragments (ions/s)	Intensity of fragments stopped in the dipole (ions/s)	Intensity of fragments stopped in the dipole left wall (ions/s)	Intensity of fragments stopped in the dipole right wall (ions/s)	Intensity of the surviving beam (ions/s)	Place where the surviving beam is stopped
12.02954	0	$7.27 \cdot 10^{11}$	0	$7.27 \cdot 10^{11}$	$4.73 \cdot 10^{11}$	DIPOLE LEFT
12.64644	$2.17 \cdot 10^7$	$7.27 \cdot 10^{11}$	0	$7.27 \cdot 10^{11}$	$4.73 \cdot 10^{11}$	DIPOLE LEFT
13.29497	$6.36 \cdot 10^8$	$7.27 \cdot 10^{11}$	$2.17 \cdot 10^7$	$7.27 \cdot 10^{11}$	$4.73 \cdot 10^{11}$	DIPOLE LEFT
13.97677	$1.60 \cdot 10^{10}$	$7.11 \cdot 10^{11}$	$6.57 \cdot 10^8$	$7.11 \cdot 10^{11}$	$4.73 \cdot 10^{11}$	DIPOLE LEFT
14.69353	$1.59 \cdot 10^{11}$	$5.68 \cdot 10^{11}$	$1.66 \cdot 10^{10}$	$5.51 \cdot 10^{11}$	$4.73 \cdot 10^{11}$	DIPOLE LEFT
15.44704	$2.38 \cdot 10^{11}$	$4.90 \cdot 10^{11}$	$1.76 \cdot 10^{11}$	$3.14 \cdot 10^{11}$	$4.73 \cdot 10^{11}$	DIPOLE LEFT
16.23919	$2.03 \cdot 10^{11}$	$5.24 \cdot 10^{11}$	$4.14 \cdot 10^{11}$	$1.11 \cdot 10^{11}$	$4.73 \cdot 10^{11}$	SLIT LEFT
17.07197	$8.96 \cdot 10^{10}$	$6.38 \cdot 10^{11}$	$6.17 \cdot 10^{11}$	$2.09 \cdot 10^{10}$	$4.73 \cdot 10^{11}$	SLIT RIGHT
17.94746	$1.94 \cdot 10^{10}$	$7.08 \cdot 10^{11}$	$7.06 \cdot 10^{11}$	$1.48 \cdot 10^9$	$4.73 \cdot 10^{11}$	DIPOLE RIGHT
18.86784	$1.45 \cdot 10^9$	$7.26 \cdot 10^{11}$	$7.26 \cdot 10^{11}$	$2.76 \cdot 10^7$	$4.73 \cdot 10^{11}$	DIPOLE RIGHT
19.83543	$1.63 \cdot 10^7$	$7.27 \cdot 10^{11}$	$7.27 \cdot 10^{11}$	$1.13 \cdot 10^7$	$4.73 \cdot 10^{11}$	DIPOLE RIGHT
20.85263	0	$7.27 \cdot 10^{11}$	$7.27 \cdot 10^{11}$	0	$4.73 \cdot 10^{11}$	DIPOLE RIGHT

## Conclusions

The work presented here belongs to a wide series of studies devoted to planning and designing the future GSI Facility. Specifically, it is related to the problem of the environmental and safety aspects, connected to the high rate of radioactivity produced.

The essential task of this work was the study of the production of radioactive nuclides in nucleus-nucleus collisions at relativistic energies. Along with it, the velocity distributions of the produced nuclides and their propagation through the Super-FRS were investigated. This knowledge is at the basis of the study of the radiation deposition in the most exposed areas of the new facility.

The work consisted in determining the yields of the residual nuclides produced in three key nuclear reactions, their velocity and their trajectories inside the first magnet of the Super-FRS. In order to do this, the nuclear-reaction Monte-Carlo code ABRABLA, developed in the last years at GSI [CHA], was opportunely implemented, introducing the description of the kinematics in the nucleus-nucleus reactions. Along with the ABRABLA code, an analysis program was made to produce the mapping of the magnetic rigidities and of the angles of the produced nuclides. This map can be used as input information for detailed ion-optical codes capable to release an exact and three-dimensional distribution of the residual nuclides around the Super-FRS target area.

The final results showed that the region around the 1<sup>st</sup> dipole of the Super-FRS will be highly radioactive: intensities with a peak up to  $8 \cdot 10^{11}$  ions/s in one spot are expected in the zone delimited by the circles of radii 7.2 m and 19.3 m in the first dipole. These ions, and the cascades of neutrons that they will generate, have to be stopped in devoted shielding structures. The map of the intensities of the produced residual nuclei has to be used as input information for appropriate transport codes with which it is possible to determine accurately the cascade of nucleons that these fluxes of ions will generate and the consequent thickness of the shielding. The surprising result found in this work – intensities up to  $10^{11}$  ions/s in the target area of the Super-FRS – would result in very thick concrete shielding and in rather high construction costs.

We like to point out that the maps of the intensities of the produced residual nuclei are of extreme importance to avoid possible quenching of the superconducting magnets, and also for the correct functioning of the magnets. In this context, also the velocity distributions of the produced ions are of great significance, since the radiation damage depends on the velocity of the ion.

## Conclusión

El presente trabajo pertenece a una amplia serie de estudios dedicados a la planificación y diseño de la futura instalación del GSI. Está relacionado específicamente con los problemas ambientales y de seguridad, conexos a su vez con el alto nivel de radioactividad producido.

La tarea esencial de este trabajo ha sido el estudio de la producción de núcleos radioactivos en reacciones núcleo-núcleo a energías relativistas. Además se han investigado las distribuciones de velocidad de los núcleos producidos y su propagación a través del Super-FRS. Este conocimiento es la base del estudio sobre la deposición de radiación en el área más expuesta de la nueva instalación.

Este Trabajo ha consistido en la determinación de la producción de núcleos residuales generados en tres reacciones nucleares clave, su velocidad y su trayectoria dentro del primer imán del Super-FRS. Para poder realizar esta tarea, el código Monte Carlo ABRABLA de simulación de reacciones nucleares, desarrollado en los últimos años en el GSI [CHA], fue oportunamente implementado introduciendo la descripción de la cinemática de las reacciones núcleo-núcleo. Además del código ABRABLA, se ha desarrollado un programa de análisis para realizar un mapa de la rigidez magnética y de los ángulos de los núcleos producidos. Este mapa puede ser usado como información inicial para códigos especializados de óptica iónica capaces de calcular distribución exacta y tridimensional de los núcleos residuales alrededor del área de la probeta del Super-FRS.

Los resultados han mostrado que la región alrededor del primer dipolo del Super-FRS será altamente radioactiva: Se esperan en un punto de la zona delimitada por los círculos de radios 7.2 m y 19.3 m intensidades con un pico de hasta  $8 \cdot 10^{11}$  iones/s. Estos iones y las cascadas de neutrones que generarán, tienen que ser paradas en estructuras blindantes específicas. El mapa de las intensidades de los núcleos residuales producidos tiene que ser usado como información inicial para códigos de transporte apropiados con los que es posible determinar con precisión la cascada de nucleones que estos flujos de iones generarán, y el consecuente espesor del blindaje. El sorprendente resultado encontrado en este trabajo – intensidades de hasta  $10^{11}$  iones/s en el

área de la probeta del Super-FRS – resultaría en blindajes muy espesos y en consecuencia costes de construcción bastante altos.

Es importante subrayar que los mapas de las intensidades de los núcleos residuales producidos son de extrema importancia para evitar posibles quenching de los imanes superconductores, y también para asegurar el correcto funcionamiento de los imanes. Asimismo, también las distribuciones de velocidad de los iones producidos son muy importantes, dado que el daño producido por la radiación depende de la velocidad del ión.

## Bibliographie

- [Abu76] A. Abul-Magd, J. Hüfner, B. Schürmann, "Friction in heavy ion reactions at relativistic energies", *Phys. Lett.* **B 60** (1976) 327
- [Ang01] N. Angert, R. Bär, W. Barth, K. Beckert, P. Beller, K. Blasche, U. Blell, O. Boine-Frankenheim, G. Breitenberger, A. Dolinskii, M. Emmerling, P. Forck, B. Franczak, G. Franchetti, B. Franzke, R. Fuchs, I. Hofmann, P. Hülsmann, W. Jacoby, K. Kaspar, J. Kaugerts, J. Klabunde, H. G. König, M. Konradt, U. Krause, B. Langenbeck, R. Lotz, G. Moritz, C. Mühle, E. Mustafin, F. Nolden, A. Peters, H. Ramakers, U. Ratzinger, H. Reich-Sprenger, V. Schaa, P. Schütt, R. Steiner, P. Spädtke, P. Spiller, M. Steck, G. Walter, Section 3 of ref. [CDR01]
- [Aum01] T. Aumann, F. Bosch, L. Chulkov, P. Egelhof, H. Emling, H. Feldmeier, H. Geissel, J. Gerl, H. Grawe, W. Henning, F. Hessberger, S. Hofmann, K. Jones, P. Kienle, Horst Lenske, G. Münzenberg, E. Roeckl, H. Schatz, M. Schädel, C. Scheidenberger, K. Schmidt, H. Simon, G. Schrieder, K. Sümmerer, H. Weick, M. Winkler, W. Trautmann, H. Wolter, Section 2.1 of ref. [CDR01]
- [Baz02] D. Bazin, O. B. Tarasov, M. Lewitowicz, O. Sorlin, "The program LISE: a simulation of fragment separators", *Nucl. Instr. Meth.* **A 482** (2002) 307
- [Ben98] J. Benlliure, A. Grewe, M. de Jong, K.-H. Schmidt, S. Zhdanov, "Calculated nuclide production yields in relativistic collisions of fissile nuclei", *Nucl. Phys.* **A 628** (1998) 458
- [Böc97] C. Böckstiegel, S. Steinhäser, J. Benlliure, H. -G. Clerc, A. Grewe, A. Heinz, M. de Jong, A. R. Junghans, J. Müller and K. -H. Schmidt, "Total kinetic energies and nuclear-charge yields in the fission of relativistic  $^{233}\text{U}$  secondary projectiles", *Phys. Lett.* **B 398** (1997) 259
- [Boh39] N. Bohr, J. A. Wheeler, "The Mechanism Of Nuclear Fission", *Phys. Rev.* **56** (1939) 426
- [Bro94] T. Brohm, K.-H. Schmidt, "Statistical Abrasion Of Nucleons From Realistic Nuclear-Matter Distributions", *Nucl. Phys.* **A 569** (1994) 821
- [CHA] CHARMS (Collaboration for High-Accuracy Experiments on Nuclear Reaction Mechanisms with the FRS); <http://www-w2k.gsi.de/kschmidt>
- [Cre70] V. P. Crespo, J. B. Cumming and J. A. M. Alexander, "Production of Tb149 from Gold by 2.2-GeV Protons", *Phys. Rev.* **C 2** (1970) 1777

- [CDR01] Conceptual Design Report, "An International Accelerator Facility for Beams of Ions and Antiprotons", Edit. H. H. Gutbrod, K. D. Groß, W. F. Henning, V. Metag, Publ. by Gesellschaft für Schwerionenforschung, November 2001
- [DeJ98] M. De Jong, K.-H. Schmidt, B. Blank, C. Boeckstiegel, T. Brohm, H.-G. Clerc, S. Czajkowski, M. Dornik, H. Geissel, A. Grewe, E. Hanelt, A. Heinz, H. Irnich, A. R. Junghans, A. Magel, G. Muenzenberg, F. Nickel, M. Pfuetzner, A. Piechaczek, C. Scheidenberger, W. Schwab, S. Steinhäuser, K. Suemmerer, W. Trinder, B. Voss, C. Ziegler, "Fragmentation cross sections of relativistic  $^{208}\text{Pb}$  projectiles", Nucl. Phys. A **628** (1998) 479
- [Feh02] G. Fehrenbacher, "Neutron Production at the GSI Fragment Separator", Workshop on Radiation Protection Issues related to Radioactive Ion Beam Facilities, CERN, Geneva, Switzerland, 30 October - 1 November 2002
- [Fel00] H. Feldmeier, J. Schnack, "Molecular Dynamics For Fermions", Rev. Mod. Phys. **72** (200) 655-688
- [Fes01] J. G. Festag, G. Fehrenbacher, Section 5 of ref. [CDR01]
- [FLU] <http://www.fluka.org>
- [FRS] <http://www-w2k.gsi.de/frs/index.asp>
- [Gai91] J.-J. Gaimard, K.-H. Schmidt, "A Reexamination Of The Abrasion-Ablation Model For The Description Of The Nuclear Fragmentation Reaction", Nucl. Phys. A **531** (1991) 709
- [GEA] <http://wwwasd.web.cern.ch/wwwasd/geant4/geant4.html>
- [Gei92] H. Geissel, P. Armbruster, K.-H. Behr, A. Bruenle, K. Burkard, M. Chen, H. Folger, B. Franczak, H. Keller, O. Klepper, B. Langenbeck, F. Nickel, E. Pfeng, M. Pfuetzner, E. Roeckl, K. Rykaczewsky, I. Schall, D. Schardt, C. Scheidenberger, K.-H. Schmidt, A. Schroeter, T. Schwab, K. Suemmerer, M. Weber, G. Muenzenberg, T. Brohm, H.-G. Clerc, M. Fauerbach, J.-J. Gaimard, A. Grewe, E. Hanelt, B. Knoedler, M. Steiner, B. Voss, J. Weckenmann, C. Ziegler, A. Magel, H. Wollnik, J.-P. Dufour, Y. Fujita, D. J. Vieira, B. Sherrill, "The Gsi Projectile Fragment Separator (FRS) - A Versatile Magnetic System For Relativistic Heavy Ions", Nucl. Instrum. Methods **B 70** (1992) 286
- [Gei03] H. Geissel, H. Weick, M. Winkler, G. Muenzenberg, V. Chichkine, M. Yavor, T. Aumann, K. H. Behr, M. Böhmer, A. Brünle, K. Burkard, J. Benlliure, D. Cortina-Gil, L. Chulkov, A. Dael, J.-E. Ducret, H. Emling, B. Franczak, J. Friese, B. Gastineau, J. Gerl, R. Gernhäuser, M. Hellström, B. Jonson, J. Kojouharova, R. Kulesa, B. Kindler, N. Kurz, B. Lommel, W. Mittig, G. Moritz, C. Mühle, J. A. Nolen, G. Nyman, P. Roussel-Chomaz, C. Scheidenberger, K.-H. Schmidt, G. Schrieder, B. M. Sherrill, H. Simon, K. Suemmerer, N. A. Tahir, V. Vysotsky, H. Wollnik, A. F. Zeller, "The Super-FRS project at GSI", Nucl. Instr. and Meth., **B 204**, (2003) 71

- [Gol74] A. S. Goldhaber, "Statistical Models Of Fragmentation Processes", Phys. Lett. **B 53** (1974) 306
- [Gra83] P. Grangé, L. Jun-Qing, and H.A. Weidenmüller, "Induced Nuclear Fission Viewed As A Diffusion Process: Transients", Phys. Rev. **C 27** (1983) 2063
- [Hui72] J. R. Huizenga, L. G. Moretto, "Nuclear Level Density", Ann. Rev. Nucl. Sci **22** (1972) 427
- [Ign75] A. V. Ignatyuk, G. N. Smirenkin, A. S. Tiskin, "Phenomenological Description Of The Energy Dependence Of The Level Density Parameter", Yad. Fiz. **21** (1975) 485 (Sov. J. Nucl. Phys. **21** (1975) 255)
- [Iwa97] N. Iwasa, H. Geissel, G. Muenzenberg, C. Scheidenberger, Th. Schwab, H. Wollnik, "MOCADI, A Universal Monte Carlo Code For The Transport Of Heavy Ions Through Matter Within Ion-Optical Systems", Nucl. Instrum. Methods **B 126** (1997) 284
- [Jun98] A. R. Junghans, M. de Jong, H.-G. Clerc, A. V. Ignatyuk, G. A. Kudyaev, K.-H. Schmidt, "Projectile-Fragment Yields As A Probe For The Collective Enhancement In The Nuclear Level Density", Nucl. Phys. **A 629** (1998) 635
- [Jur02] B. Jurado Apruzzese, PhD Thesis, "New signatures on dissipation at small deformations from studies of fission induced by peripheral heavy-ion collisions at relativistic energies", Universidad de Santiago de Compostela, Facultad de Física, Departamento de Física de Partículas, Santiago de Compostela, Spain, June 2002
- [Kra40] H.A. Kramers, "Brownian Motion In A Field Of Force And The Diffusion Model Of Chemical Reactions", Physika VII **4** (1940) 284
- [LCS] <http://www-xdiv.lanl.gov/XCI/PROJECTS/LCS/index.html>
- [Mor75] L. G. Moretto, "Statistical Emission Of Large Fragments: A General Theoretical Approach", Nucl. Phys. **A 247** (1975) 211
- [Mor89] D. J. Morrissey, "Systematics Of Momentum Distributions From Reactions With Relativistic Ions", Phys. Rev. **C 39** (1989) 460.
- [PLI] <http://www-306.ibm.com/software/awdtools/pli>
- [R3B] <http://www-land.gsi.de/r3b>
- [Ric03] M. V. Ricciardi, T. Enqvist, J. Pereira, J. Benlliure, M. Bernas, E. Casarejos, V. Henzl, A. Kelic, J. Taieb, K.-H. Schmidt, "Experimental Indications For The Response Of The Spectator To The Participant Blast", Phys. Rev. Lett. **90** (2003) 212302

- [Röh94] C.Röhl, PhD Thesis, „Experimentelle Möglichkeiten zur Niederenergiespaltung relativistscher exotischer Aktiniden an der GSI“, TU Darmstadt, Institut für Kernphysik, Darmstadt, Germany, December 1994
- [SAT] <http://www-w2k.gsi.de/kschmidt/SATAN>
- [Sch93] K.-H. Schmidt, T. Brohm, H.-G. Clerc, M. Dornik, M. Fauerbach, H. Geissel, A. Grewe, E. Hanelt, A. Junghans, A. Magel, W. Morawek, G. Muenzenberg, F. Nickel, M. Pfuetzner, C. Scheidenberger, K. Suemmerer, D. Vieira, B. Voss, C. Ziegler, “Distribution Of Ir And Pt Isotopes Produced As Fragments Of 1 A Gev 197au Projectiles - A Thermometer For Peripheral Nuclear Collisions”, Phys. Lett. **B 300** (1993) 313
- [Sch96] A. Schüttauf, Phd Thesis, “Untersuchung der Kernfragmentation”, Universität Frankfurt, 1996
- [Sch97] K.-H. Schmidt, E. Hanelt, H. Geissel, G. Muenzenberg, J.-P. Dufour, "The Momentum-Loss Achromat - A New Method For The Isotopical Separation Of Relativistic Heavy Ions", Nucl. Instr. Meth. **A 260** (1987) 287
- [Sch02] K.-H. Schmidt, M. V. Ricciardi, A. Botvina, T. Enqvist, “Production Of Neutron-Rich Heavy Residues And The Freeze-Out Temperature In The Fragmentation Of Relativistic <sup>238</sup>U Projectiles Determined By The Isospin Thermometer”, Nucl. Phys. **A 710** (2002) 157
- [SFRS] [http://www-new.gsi.de/zukunftsprojekt/experimente/superfrs/index\\_e.html](http://www-new.gsi.de/zukunftsprojekt/experimente/superfrs/index_e.html)
- [SHI] <http://www.kfki.hu/~ionhp/doc/prog/shield.htm>
- [Sie86] A. J. Sierk, "Macroscopic Model Of Rotating Nuclei", Phys. Rev. **C 33** (1986) 2039
- [Sim64] J. A. Simpson, “High resolution, low energy electron spectrometer”, Rev. Sci. Instrum. **35** (1964) 1698
- [Wei37] V. F. Weisskopf, "Statistics And Nuclear Reactions", Phys. Rev. **52** (1937) 295
- [Wei04] Helmut Weick, GSI, private communication, 2004.
- [Wil76] B. D. Wilkins, E. P. Steinberg, R. R. Cashman, “Scission-point model of nuclear fission based on deformed-shell effects”, Phys. Rev. **C 14** (1976) 1832